nature chemistry

Article

https://doi.org/10.1038/s41557-025-01886-w

Quantitative profiling of lipid transport between organelles enabled by subcellular photocatalytic labelling

Received: 3 January 2024

Accepted: 25 June 2025

Published online: 6 August 2025

Check for updates

Xi Chen[1,2,7], Ru He[3,4,7], Haolin Xiong[1,2], Ruohong Wang[1,2], Yandong Yin[1], Yiyun Chen[3,4,5] ✉ & Zheng-Jiang Zhu[1,6] ✉

Subcellular lipid composition and transport substantially influence the physiological and pathological functions of both cells and organelles. However, lipid transport and turnover between organelles remain poorly understood due to a lack of methods for selectively labelling lipids in organelles. Here we develop a subcellular photocatalytic labelling strategy that enables organelle-selective lipid analysis by mass spectrometry and the quantitative profiling of lipid transport between organelles. We use this approach to quantitatively characterize fatty-acyl-dependent transport of phosphatidylethanolamine and phosphatidylserine lipids between the endoplasmic reticulum and mitochondria, the nucleus or lysosomes. Further experiments revealed the relative contributions of various biosynthesis pathways to the phosphatidylethanolamine and phosphatidylserine lipid compositions in the mitochondria, nucleus and lysosomes. Lysosome-specific photocatalytic labelling revealed the impact of the mTOR kinase pathway on lysosomal lipid metabolism. Together, this subcellularly localized photocatalytic labelling of lipids quantitatively deciphers the subcellular lipid composition and transport, enhancing our understanding of lipid metabolism in living organisms.

Lipids represent a distinctive class of biomolecules within cells and form the bilayer membrane of organelles in the cytoplasm[1,2]. These membrane-bound organelles establish chemically and physically distinct compartments that regulate diverse cellular activities. The lipid composition of different organelles critically influences their physiological and pathological functions, underscoring the importance of lipidomic analysis at the organelle level[3,4]. Traditional technologies often involve organelle isolation and separation using high-speed centrifugation or affinity-based purification, followed by mass spectrometry analysis[5]. However, these methods are time-consuming, and isolating organelles from their physiological environment markedly alters their metabolism. In eukaryotic cells, most lipids are de novo synthesized in the endoplasmic reticulum (ER) and then transported to other organelles[6]. Lipid transport between organelles is indispensable for maintaining cellular structure, energy balance and signalling pathways. Dysregulation in lipid transport contributes to major human diseases, including metabolic diseases, neurodegenerative diseases and lipid storage disorders[7]. While lipid transport is a fundamental mechanism

[1]Interdisciplinary Research Center on Biology and Chemistry, Shanghai Institute of Organic Chemistry, Chinese Academy of Sciences, Shanghai, China. [2]University of Chinese Academy of Sciences, Beijing, China. [3]State Key Laboratory of Chemical Biology, Shanghai Institute of Organic Chemistry, University of Chinese Academy of Sciences, Chinese Academy of Sciences, Shanghai, China. [4]School of Physical Science and Technology, ShanghaiTech University, Shanghai, China. [5]School of Chemistry and Material Sciences, Hangzhou Institute for Advanced Study, University of Chinese Academy of Sciences, Hangzhou, China. [6]Shanghai Key Laboratory of Aging Studies, Shanghai, China. [7]These authors contributed equally: Xi Chen, Ru He. ✉e-mail: yiyunchen@sioc.ac.cn; jiangzhu@sioc.ac.cn

for maintaining organismal homeostasis, the understanding of the subcellular transport of lipids requires further improvement. This is mainly due to a lack of technologies that enable the quantitative and dynamic profiling of lipid transport in live cells.

Traditionally, the study of lipid transport between organelles relies on radiolabelling technology (for example, ^{3}H) coupled with organelle isolation[8,9]. Recently, alternative lipid labelling methodologies have emerged that use fluorophore tagging, click chemistry tagging and mass tagging to study cellular lipid metabolism and transport dynamics in live cells. Fluorophore tagging employs fluorescent probes to label specific lipid classes (for example, sphingosine) in live cells[10–12], enabling subcellular lipid tracing. Click chemistry tagging involves introducing an azide or alkyne group into lipids[13,14], which reacts with reporter groups for subcellular lipid labelling. For example, Tamura et al.[13] incorporated azido-choline into phosphatidylcholine lipids and selectively labelled them via the organelle-selective click chemistry reaction. Mass tagging, such as by the METALIC method[15], employs two enzymes to add distinct mass tags to lipids in donor and acceptor organelles, facilitating quantitative profiling of lipid exchanges between the ER and mitochondria. However, most of these strategies introduce chemical modifications into lipid structures, potentially influencing their subcellular distribution, inter-organelle transport and cellular metabolism in live cells.

Proximity labelling has gained widespread application in profiling the subcellular compartmentalization and interactions of biomacromolecules (for example, proteins)[16–18]. This technology employs enzymes to catalyse the generation of reactive species in close proximity to a target, enabling rapid and efficient labelling of proteins within specific subcellular regions[16–19]. Recently, chemists have embraced the concept of proximity labelling by employing photocatalysts and light as artificial enzymes[17,18,20,21]. For example, we and others have used small-molecule photocatalysts, such as organic dyes[22–24] and metal complexes[25–27], to generate reactive species and label proteins in subcellular compartments. However, current applications of proximity labelling technology predominantly focus on proteins. Extending proximity labelling to characterizing the subcellular compartmentalization of lipids in live cells remains challenging due to their versatile chemical structures and a lack of enrichment strategy. The hydrophobicity of lipids also restricts their spatial distribution within the membrane environment, hindering the common proximity labelling reactions.

In this study we developed a subcellularly localized photocatalytic proximity labelling strategy for organelle-selective lipid analysis by mass spectrometry (Fig. 1a). Organelle-selective organic dyes were employed to absorb light and catalyse the generation of reactive species from labelling probes. The rationally designed labelling probe, facilitating hydrophobic interactions with lipids, enables efficient and selective proximity labelling of lipids. The technology facilitates spatially resolved investigation of subcellular lipid compositions and is employed to quantitatively profile lipid transport and turnover between the ER and mitochondria, the nucleus or lysosomes.

Results

Design of photocatalytic labelling reactions for lipids

Recently, photocatalysts have been developed as artificial enzymes, leveraging visible light irradiation to catalyse proximity-dependent labelling reactions of proteins within live cells. However, the extension of this labelling strategy to characterize the subcellular compartmentalization of lipids in live cells has not been previously reported. Inspired by our prior research[23], we tailored a photoactivated azide labelling probe, phenyl azide–alkyl–tertiary amine (AzPh–alkyl–TA), specifically designed for the photocatalytic labelling of lipids using organic dyes as photocatalysts (Fig. 1a). The AzPh–alkyl–TA probe consisted of three functional substructures, including a reactive group, a hydrophobic linker and an ionization enhancer for mass spectrometry (MS) analysis. Upon exposure to blue light irradiation (wavelength λ = 468 nm), the aryl azide in the reactive group was activated to triplet nitrenes by photosensitizers. These activated nitrenes could rearrange to ketenimine intermediates and promptly couple with the nucleophilic head groups of lipids, such as phosphatidylethanolamine (PE) and phosphatidylserine (PS) lipids (Fig. 1a). Notably, the hydrophobic linker enhanced the lipophilicity of AzPh–alkyl–TA, facilitating its interaction with the lipid bilayer membrane of subcellular organelles.

To demonstrate the photocatalytic reactions between the AzPh–alkyl–TA probe and lipids, we prepared liposomes by mixing dioleoylphosphatidylcholine (DOPC) with various lipid standards in phosphate-buffered saline (PBS). Common organic dyes, including rhodamine 123 (Rh 123), acridine orange (AO) and fluorescein, were chosen as photocatalysts[23]. The liposome, photocatalyst and AzPh–alkyl–TA were mixed and exposed to blue light irradiation (Extended Data Fig. 1a). Subsequently, we conducted liquid chromatography–mass spectrometry (LC-MS) analyses of the AzPh–alkyl–TA-labelled lipids after irradiation, and their intensities were used to quantify the relative labelling efficiencies (that is, reactivities) for different lipids. Our results revealed that lipids with nucleophilic head groups, such as PE, PS, sphingosine (Sph), lysoPE (LPE) and lysoPS (LPS), exhibited higher reactivities than neutral lipids like phosphatidylcholine, sphingomyelin and cholesterol for different organic dyes (Fig. 1b). MS/MS spectra of the AzPh–alkyl–TA-labelled lipids provided unequivocal evidence of the formation of photocatalytically labelled lipids (PL lipids) reacting on their head groups (Supplementary Fig. 1). Control experiments in the absence of photocatalyst, labelling probe, blue light irradiation or liposome were also conducted and measured by LC-MS to confirm that the successful photocatalytic labelling of lipids required all of the indicated components (Extended Data Fig. 1b). Critically, the labelling probe (in organic solvents like acetonitrile) showed no reactivity towards lipids even in the presence of organic dyes and light irradiation, demonstrating that the liposome environment is essential for productive labelling chemistry.

Organelle-selective photocatalytic lipid labelling in cells

Next we expanded the photocatalytic labelling of lipids to subcellular organelles in live cells. Organic dyes, such as Rh 123, known for their biocompatibility and selective localization in mitochondria in live cells, were employed[28]. We conducted the mitochondria-specific photocatalytic labelling of lipids in HeLa cells by sequentially incubating Rh 123 and the AzPh–alkyl–TA probe, followed by blue light irradiation. After irradiation, the PL lipids were measured by LC-MS. In total, 64 PL lipids covering seven lipid classes were measured with this mitochondria-specific photocatalytic labelling reaction (Fig. 2a). We systematically evaluated the conditions that may affect the photocatalytic labelling. The hydrophobic linker of probes with more than ten carbons turned out to have high reactivity (Extended Data Fig. 2a,b). Additionally, the concentration and incubation time of organic dye and probe had slight effects on reactivity. The reactivity was increased with longer irradiation time (Extended Data Fig. 2c–h). We also assessed cell viability and found no significant cytotoxicity after the photocatalytic labelling with Rh 123 (Extended Data Fig. 3a), confirming the biocompatibility of the photocatalytic labelling reaction.

We further employed confocal microscopy to validate the mitochondria localization of the photocatalytically labelled products (PL products). For this purpose, we used an AzPh–alkyne probe and employed biotin–PEG3 (polyethylene glycol with three repeating units)–azide to couple with the AzPh–alkyne probe via the click chemistry reaction, and then used Cy5 (cyanine 5)–streptavidin to visualize the subcellular distribution of PL products after the photocatalytic labelling reaction. The results demonstrated excellent co-localization of the PL products with the mitochondria-localized protein TOMM20 (Fig. 2b). The Pearson's R value was determined to be 0.87 (Extended Data Fig. 3b). We used the AzPh–alkyne probe in combination with UV-light-induced photoaffinity labelling chemistry[29] to visualize the

https://doi.org/10.1038/s41557-025-01886-w

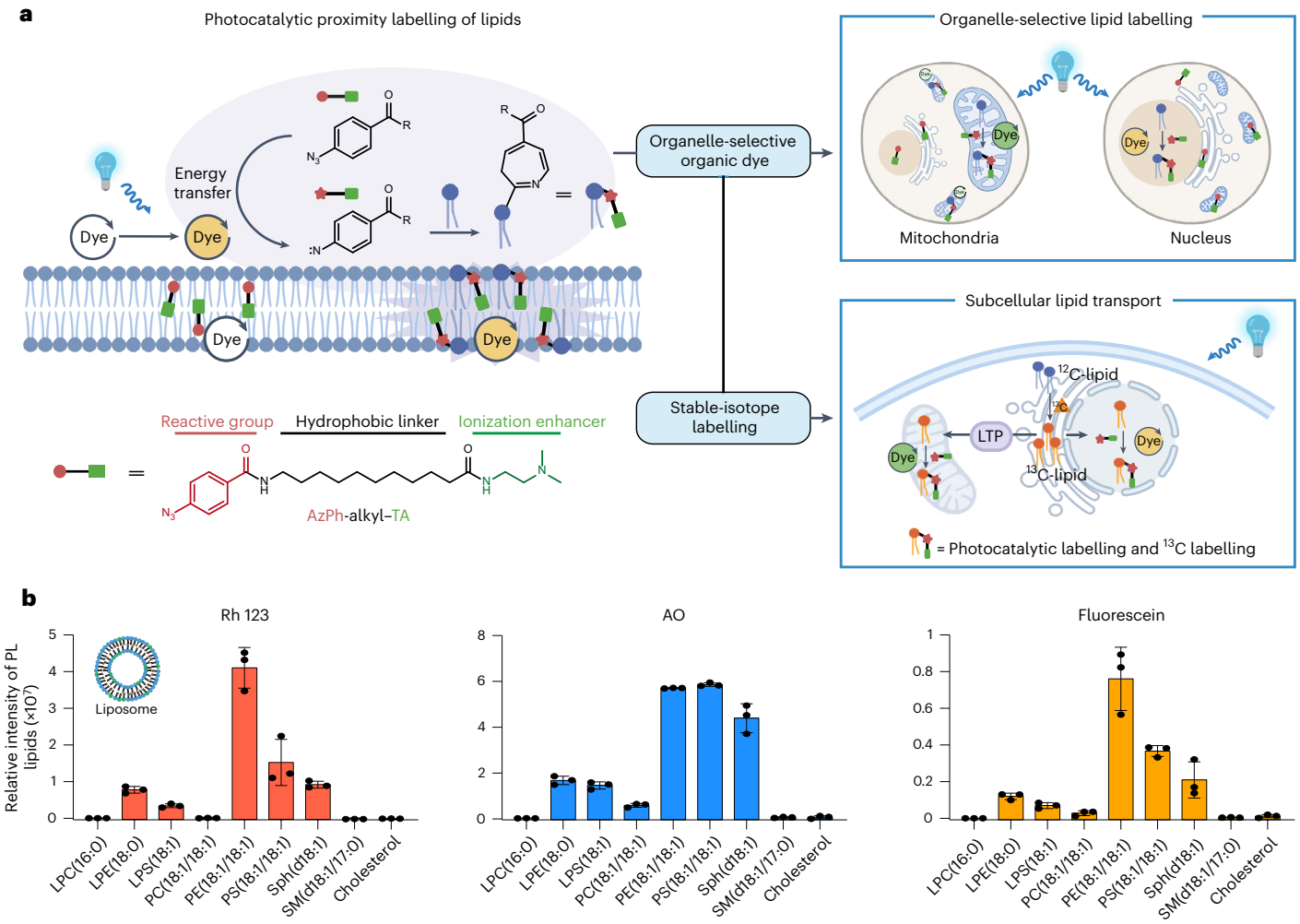

Fig. 1 | Photocatalytic labelling of lipids with organic dyes as photocatalysts. **a**, Schematic illustrations of the photocatalytic proximity labelling reaction for lipids, the structural design of the labelling probe and related applications in organelle-selective lipid labelling and subcellular lipid transport between organelles. **b**, Relative intensities of PL lipids measured by LC-MS using different dyes as photocatalysts: Rh 123 (left), AO (middle) and fluorescein (right). Each indicated lipid was 10 nmol in the liposome solution. The inset shows a liposome. Bar plots represent mean ± s.d. ($n = 3$ independent replicates). PC, phosphatidylcholine; LPC, lysoPC; SM, sphingomyelin. Panel **a** created with BioRender.com.

probe's distribution within the cells. The results demonstrated that the probe was ubiquitously distributed throughout the cells without organelle selectivity. This finding indicated that organelle selectivity is achieved primarily through the application of photosensitizers rather than the probe itself (Extended Data Fig. 3c). Control experiments conducted without blue light irradiation or the organic dye yielded no fluorescent signals from PL products (Extended Data Fig. 3d). Similarly, control experiments in the absence of Rh123, labelling probe or blue light irradiation were also conducted and measured by LC-MS to confirm that the successful labelling of lipids in cells required all of the indicated components (Extended Data Fig. 4).

AO is an organic dye with selective nucleus localization[30]. We expanded our method for nucleus-selective photocatalytic labelling of lipids in HeLa cells using AO as the photocatalyst. Similarly, 74 PL lipids covering seven lipid classes with nucleophilic head groups were detected (Fig. 2c). No significant cytotoxicity was observed after the photocatalytic labelling with AO, confirming the biocompatibility of the photocatalytic labelling reaction with AO (Extended Data Fig. 3a). Confocal microscopy confirmed robust co-localization between PL products and the nuclear marker histone H3 (Fig. 2d). Quantification of fluorescence overlap revealed a strong correlation (Pearson's $R = 0.86$; Extended Data Fig. 3b). Similar control experiments conducted without blue light irradiation or AO dye yielded no fluorescent signals from the PL products (Extended Data Fig. 3d). Co-localization with AO staining also showed comparable spatial overlap (Supplementary Fig. 2a,b).

DND-189 is an organic dye with lysosome-specific localization[31] and enables successful lysosome-specific lipid labelling. A total of 79 PL lipids spanning seven lipid classes were detected (Fig. 2e). The photocatalytic labelling with DND-189 exhibited no significant cytotoxicity, confirming the biocompatibility of the reaction (Extended Data Fig. 3a). Confocal microscopy similarly confirmed robust co-localization of PL products with the lysosomal marker LAMP1 (Fig. 2f), with a Pearson's R value of 0.83 (Extended Data Fig. 3b). Control experiments omitting either blue light irradiation or the lysosomal dye DND-189 showed no detectable PL-product signals (Extended Data Fig. 3d). Further validation via live-cell imaging with the lysosome-specific dye DND-99 revealed strong spatial overlap (Supplementary Fig. 2c,d), aligning with our lysosomal targeting observations and reinforcing the method's reproducibility across dynamic cellular conditions.

To further validate the specificity of organelle-selective proximity labelling of lipids, we conducted a comparative analysis of the relative intensities of three PE lipids and three PS lipids obtained

https://doi.org/10.1038/s41557-025-01886-w

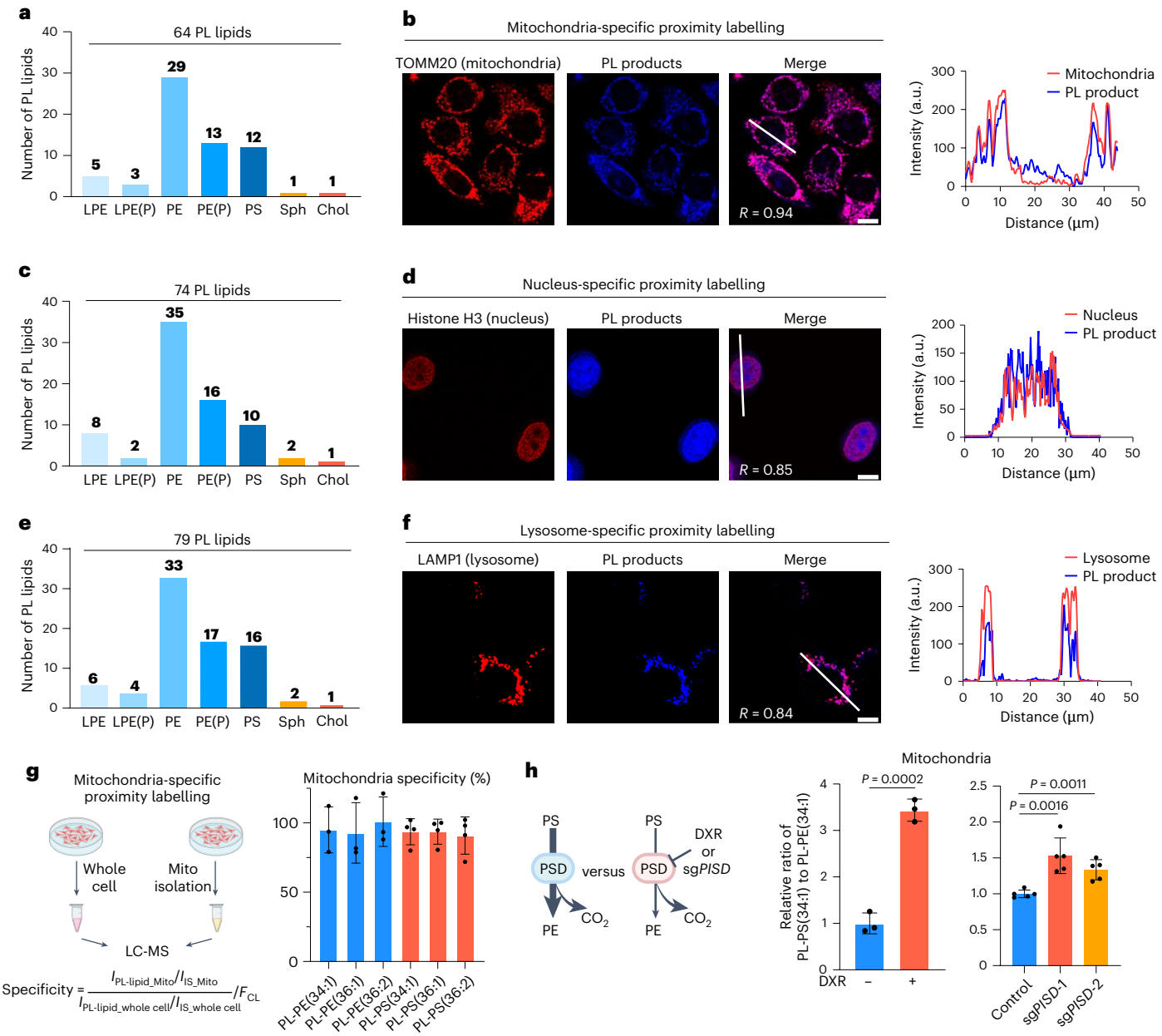

Fig. 2 | Organelle-selective photocatalytic labelling of lipids in live cells. **a**,**c**,**e**, Number of PL lipids in the mitochondria (**a**), nucleus (**c**) and lysosomes (**e**) of HeLa cells, respectively. Chol, cholesterol. **b**,**d**,**f**, Representative fluorescent images of mitochondria-specific (**b**), nucleus-specific (**d**) and lysosome-specific photocatalytic labelling (**f**) of lipids in HeLa cells, respectively (scale bars, 10 μm). An AzPh–alkyne probe was used as the labelling probe (Methods). The intensity plots at the right were measured along the white lines in **b**, **d** and **f**. **g**, Comparative analyses of the relative intensities of three PE and three PS lipid species obtained through mitochondria-specific photocatalytic labelling (PL-lipid) and traditional mitochondria isolation, in the mitochondria (Mito) and whole cell. Refer to the Supplementary Information, 'General Methods', for the calculation and definition of specificity. Bar plots represent mean ± s.d. ($n = 3$ and 4 biologically independent replicates for PE and PS species, respectively). **h**, Mitochondria-specific inhibition of PE biosynthesis via DXR-induced inhibition of PSD or sg*PISD* (single guide RNA targeting the *PISD* gene) induction. Bar plots represent mean ± s.d. ($n = 3$ and 5 biologically independent replicates for DXR and sg*PISD* inductions, respectively; two-tailed Student's *t*-test). HeLa cells were treated with DXR (5 μM) for 24 h. Illustrations in **g** and **h** created with BioRender.com.

through mitochondria-specific proximity labelling and traditional mitochondria isolation. The average specificities for PE and PS lipid species were 96 ± 4% and 93 ± 1%, respectively (Fig. 2g). Previously, Bellance et al.[32] reported that doxorubicin (DXR) specifically inhibited phosphatidylserine decarboxylase (PSD) activity in mitochondria, resulting in an increased PS/PE ratio in isolated mitochondria. We sought to replicate this experiment using the mitochondria-specific proximity labelling strategy. Upon DXR treatment in HeLa cells, the relative ratio of PL-PS (34:1) to PL-PE (34:1) in mitochondria was significantly higher than that of the control group (Fig. 2h, middle). However, as an anticancer drug, DXR is known to affect cytotoxicity and various metabolic pathways. To further validate the mitochondria specificity of the photocatalytic labelling, we generated *PISD* (the gene encoding PSD) knock-out HeLa cells using the CRISPR-Cas9 technique (Supplementary Fig. 3). Similarly, the relative ratio of PL-PS (34:1) to PL-PE (34:1) in *PISD* knock-out HeLa cells is significantly higher than that of the HeLa wild-type cells (Fig. 2h, right). Taken together, these results demonstrated the remarkable organelle specificity achieved through photocatalyst-based proximity labelling of lipids in live cells.

Lipid transport profiling from ER to mitochondria

In eukaryotic cells, most phospholipids are de novo synthesized in the ER and then transported to other organelles. For example, PS is biosynthesized from a head-exchange reaction between serine and PE or phosphatidylcholine in the ER and then transported to the mitochondria (Fig. 3a). Once shuttled to the mitochondria, PS is rapidly converted to PE, a conversion catalysed by PSD[33]. To characterize lipid transport from the ER to mitochondria, we devised a dual-labelling strategy that integrated stable-isotope labelling in the ER and photocatalytic proximity labelling in mitochondria. Specifically, HeLa cells were treated with uniformly ^{13}C-labelled serine ([U-^{13}C]-serine) to label newly synthesized PS lipids ($^{13}C_3$-PS) in the ER. Once transported to the mitochondria, both $^{13}C_3$-PS and its product $^{13}C_2$-PE could be selectively labelled by the AzPh–alkyl–TA probe, catalysed by Rh 123 and light irradiation. Subsequently, HeLa cells were collected for lipid extraction, and the dual-labelled lipids (PL-^{13}C-PS and PL-^{13}C-PE) were analysed using LC-MS. To validate our technology, we replicated the DXR inhibition experiment. The results demonstrated that normalized intensities of dual-labelled PE lipids, such as PL-^{13}C-PE(16:0_18:1) and PL-^{13}C-PE(18:0_18:1), were significantly lower in the DXR-treated group (Fig. 3b). We also conducted the dual-labelled reaction in HeLa cells with *PISD* knock-out. Similarly, the normalized intensityies of PL-^{13}C-PE(16:0_18:1) and PL-^{13}C-PE(18:0_18:1) were significantly lower in the PSD deficiency groups (Fig. 3c). The results proved that the newly synthesized PS lipids in the ER could be transported to mitochondria and converted into PE lipids.

Pulse-chase labelling with radiolabelling techniques has been used for the study of kinetics of lipid transport. A fraction of newly synthesized lipids is labelled through a pulse, followed by chase experiments to quantify inter-organelle lipid transport kinetics at the molecular level. In our study, the dual-labelling strategy was first combined with a pulse-chase experiment to characterize lipid transport kinetics between the ER and mitochondria. HeLa cells were pulse labelled with [U-^{13}C]-serine, followed by chases with unlabelled serine for 15, 30, 45, 60, 90 and 120 min. Simultaneously, photocatalytic proximity labelling of lipids in the mitochondria was conducted at varying chase-time intervals. Given that PS that originates from the ER is rapidly converted to PE, catalysed by PSD, we specifically quantified the intensity changes of dual-labelled PE(18:0_20:4) and PE(18:1_18:1) over the chase time. Consistent with the previous study[34], PS transport from the ER to mitochondria is a rapid process, occurring within approximately 1 h (Fig. 3d). We characterized the rate of lipid transport from the ER to mitochondria by measuring the change in dual-labelled PE in the mitochondria per hour. PL-^{13}C-PE(18:0_20:4) increased rapidly for 60 min with a change speed of 2.3×10^5 h^{-1}. The PL-^{13}C-PE(18:1_18:1) increased relatively slowly, with a speed of 5.3×10^4 h^{-1}. Notably, the total cellular abundance of ^{13}C-PE species remained largely unchanged during the chase period (Supplementary Fig. 4), which indicated that mitochondrial pulse-chase labelling reflects lipid transport rather than changes in whole-cell PE lipid synthesis.

As the newly synthesized lipids are continually produced in the ER and transported to targeted organelles, the photocatalytic labelling method could measure newly synthesized lipids in target organelles, quantifying the turnover rate of lipid pools at the lipid population level. To further quantitatively profile the kinetics of lipid turnover from the ER to mitochondria, we conducted continuous stable-isotope labelling for up to 72 h in HeLa cells using [U-^{13}C]-serine and then applied photocatalytic proximity labelling in mitochondria at different time intervals (Fig. 3e, top). Throughout the continuous labelling period, the tracer availability was sufficient and the metabolic status of the mitochondria remained stable (Supplementary Fig. 5). A total of 18 dual-labelled PE lipids (PL-^{13}C-PE) at six time points were measured and subjected to hierarchical cluster analysis (Fig. 3f). The dynamic turnovers of newly synthesized PE lipids in mitochondria were categorized into high-turnover and low-turnover groups. In the high-turnover group, newly synthesized PE lipids, such as PE(18:0_22:6), accumulated about 70% of their total amounts in mitochondria after 72 h. By comparison, other newly synthesized PE lipids, such as PE(18:1_22:6), differing in one fatty acyl chain, exhibited an accumulation of roughly 40% of their total amounts in mitochondria after 72 h. These results disclosed a fatty-acyl-dependent turnover pattern of newly synthesized PE lipids in mitochondria. Given that the conversion of PS to PE, catalysed by PSD, is rapid and non-rate-limiting, we speculated that the observed fatty-acyl-dependent turnover of PE lipids in mitochondria stems from distinct transport kinetics of their precursor PS lipids from the ER to mitochondria.

We further employed the first-order exponential function to quantitatively fit the turnover kinetics of the newly synthesized PE lipids in mitochondria (Fig. 3e and Supplementary Fig. 6). The apparent first-order constant k represents the turnover rate, while the amplitude a represents the maximum turnover fraction. In addition, $t_{1/2}$, which is inversely proportional to k, represents the half-time required to reach the maximum turnover fraction. Taking PL-^{13}C-PE(18:0_20:4) in the high-turnover group as an example, the turnover fraction gradually increased to 0.70 within 72 h. The fitted rate k was calculated as 0.05 h^{-1} with an R^2 value of 0.99. For PL-^{13}C-PE(18:1_18:1) in the low-turnover group, the turnover fraction was gradually increased to 0.43 within 72 h. Accordingly, the fitted turnover rate k was calculated as 0.03 h^{-1}, which is lower than that of PL-^{13}C-PE(18:0_20:4) (Fig. 3e, bottom). The turnover rates in continuous labelling were consistent with the lipid transport

Fig. 3 | Quantitative profiling of lipid transport from ER to mitochondria. **a**, Schematic illustration of LTP-mediated PS transport from the ER to the mitochondria and PE biosynthesis by PSD in the mitochondria. PSS, phosphatidylserine synthases. **b**, Mitochondria-specific inhibition of PE biosynthesis by DXR characterized by the photocatalytic proximity labelling. Bar plots represent mean ± s.d. (n = 6 biologically independent replicates per group; two-tailed Student's t-test). HeLa cells were treated with DXR (5 μM) for 24 h. DMSO, dimethyl sulfoxide. **c**, PSD enzyme deficiency in HeLa cells characterized by the dual-labelled PE lipids. Bar plots represent mean ± s.d. (n = 6 biologically independent replicates per group; two-tailed Student's t-test). **d**, Top: the pulse-chase labelling of lipids was performed using [U-^{13}C]-serine, followed by a chase with unlabelled serine. Photocatalytic proximity labelling of lipids in the mitochondria of HeLa cells was conducted at varying chase-time intervals. Bottom: the intensity changes (ΔI) of dual-labelled PE(18:0_20:4) and PE(18:1_18:1) over the chase time (t) were plotted. The red dots indicate the time point at 60 min during the chase, which was used to calculate the change in speed ($\Delta I/\Delta t$) for each lipid. Error bars represent mean ± s.e.m. (n = 6 biologically independent replicates per group). **e**, Top: the continuous stable-isotope labelling of lipids in the ER using [U-^{13}C]-serine and the photocatalytic proximity labelling of lipids in mitochondria of HeLa cells at different time intervals. Bottom: the quantitative fit of the turnover kinetics of newly synthesized PE lipids in mitochondria using the first-order exponential function: PE(18:0_20:4) and PE(18:1_18:1). Red dots represent the median value from four biologically independent replicates for 0 h, 6 h, 12 h, 24 h and 72 h, and from three biologically independent replicates for 48 h. **f**, Hierarchical clustering analysis of 18 dual-labelled PE lipids (PL-^{13}C-PE) accumulated in mitochondria of HeLa cells. The fraction represents the ratio of newly synthesized PE to its total amount in mitochondria. **g**, Relative percentages of newly synthesized PE lipids from the PSD pathway in mitochondria. The red arrow indicates the relative percentage of five predominant PE lipids in mitochondria biosynthesized from the PSD pathway. **h**, The contribution percentage of the PSD biosynthesis pathway to the PE lipid pool in mitochondria. Bar plots represent median ± s.d. (n = 4 biologically independent replicates). **i**, Schematic illustration of lipid transport from donor to acceptor by LTPs. **j**, The effects of LTP deficiency (such as VPS13A and PDZD8) on lipid transport from the ER to mitochondria in HeLa cells. Bar plots represent mean ± s.e.m. (n = 6 biologically independent replicates per group; two-tailed Student's t-test). NC, negative control. Illustrations in **a**, **d**, **e** and **i** created with BioRender.com.

rates in pulse-chase labelling (Fig. 3d,e). Notably, the maximum turnover fractions represent the proportions of PE lipids biosynthesized via the PSD pathway in mitochondria. After 72 h, the turnovers of most newly synthesized PE lipids reached a maximum and demonstrated a fatty-acyl-dependent turnover pattern (Supplementary Fig. 6).

Finally, we quantified relative percentages of newly synthesized PE lipids from the PSD pathway in mitochondria after 72 h (Fig. 3g). Notably, among the 18 dual-labelled PE lipids analysed, PE(18:0_18:1) emerged as the most abundant one, accounting for 23.4% of the total PE lipids. PE(16:0_18:1), PE(18:0_20:4), PE(18:1_18:1) and PE(18:0_22:6) constituted other major PE lipids biosynthesized from PS lipids via the PSD pathway. Remarkably, these five predominant PE lipids collectively represented approximately 80.5% of the total PE lipids biosynthesized from the PSD pathway (Fig. 3g). Further quantification revealed that 18 PE lipids biosynthesized via the PSD pathway accounted for 59.9% of the total PE lipids present in mitochondria (Fig. 3h and Extended Data Fig. 5).

We further evaluated the impact of lipid transfer proteins on ER-to-mitochondria lipid transport with a dual-labelling strategy. We used lipid transfer protein (LTP)-deficient HeLa cells and assayed the relative intensity of major PS lipids transported from the ER to mitochondria (Fig. 3i). VPS13A, a known lipid transporter between the ER and mitochondria, was found to play a key role in this process[35]. In *VPS13A* knock-down cells, the relative intensities of PL-^{13}C-PE(16:0_18:1), PL-^{13}C-PE(18:1_18:1) and PL-^{13}C-PE(18:0_20:4) were significantly reduced in both continuous stable-isotope labelling and pulse-chase labelling, indicating impaired PS transport from the ER to mitochondria (Fig. 3j and Supplementary Fig. 7). PDZD8, a protein containing the

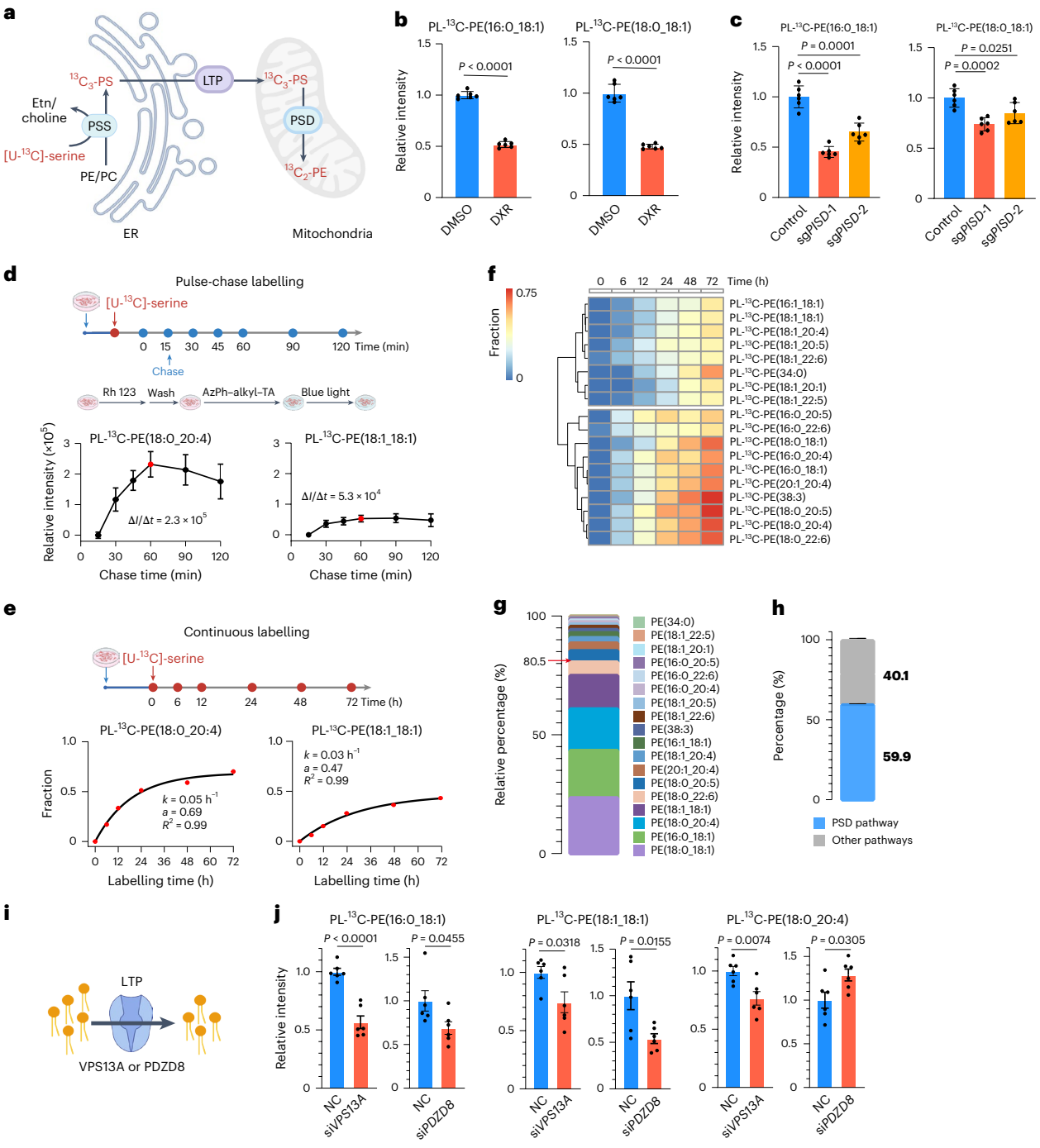

https://doi.org/10.1038/s41557-025-01886-w

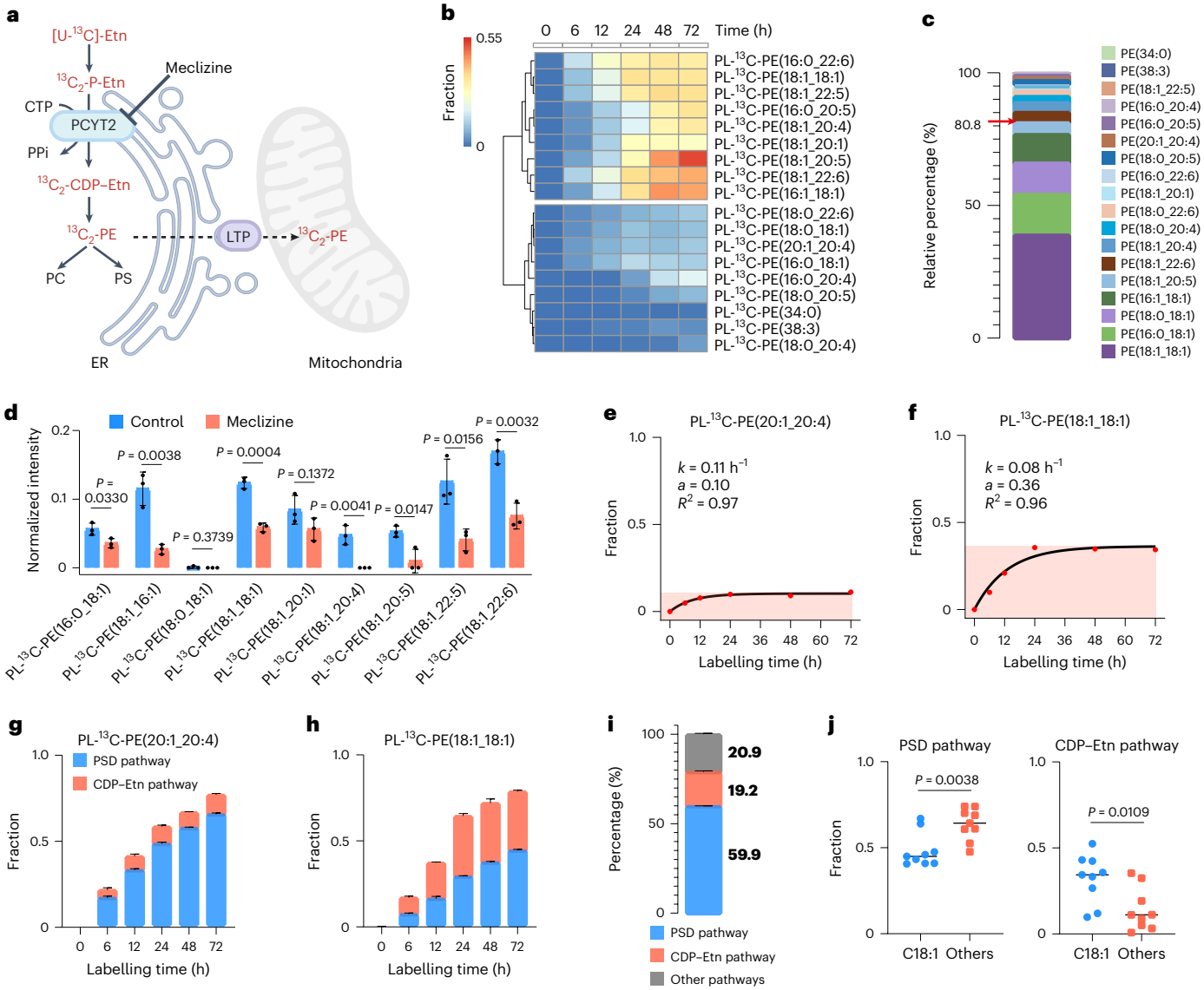

Fig. 4 | Quantitative profiling of PE lipid turnover from ER to mitochondria. **a**, Schematic illustration of PE biosynthesis via the CDP–Etn pathway in ER and possible transportation from the ER to mitochondria. P-Etn, phosphoethanolamine; CTP, cytosine triphosphate; PPi, pyrophosphate. **b**, Hierarchical clustering analysis of 18 dual-labelled PE lipids (PL-^{13}C-PE) accumulated in mitochondria of HeLa cells. **c**, Relative percentages of newly synthesized PE lipids in mitochondria biosynthesized from the CDP–Etn pathway in ER. The red arrow indicates the relative percentage of five predominant PE lipids in mitochondria biosynthesized from the CDP–Etn pathway. **d**, ER-specific inhibition of PE biosynthesis via meclizine-induced inhibition of PCYT2 characterized by photocatalytic proximity labelling. Bar plots represent mean ± s.d. ($n = 3$ biologically independent replicates for each group; two-tailed Student's t-test). HeLa cells were treated with meclizine (50 μM) for 6 h. **e**,**f**, The quantitative fit of the turnover kinetics of newly synthesized PE lipids in mitochondria using the first-order exponential function. Red dots represent the median value from four biologically independent replicates. The shaded regions indicate the fraction of dual-labelled lipids at the 72 h time point. **g**,**h**, The integrated accumulations of PE(20:1_20:4) (**g**) and PE(18:1_18:1) (**h**) originating from the PSD pathway and CDP–Etn pathway, respectively. **i**, Contribution percentages of PE biosynthesis pathways to the PE pool in mitochondria. Bar plots represent median ± s.d. ($n = 4$ biologically independent replicates for each pathway in **g**–**i**, except for the PSD pathway at 48 h, which includes three biologically independent replicates). **j**, The turnover fractions of PE lipids in mitochondria with or without a C18:1 fatty acyl chain were assessed after 72 h for the PSD pathway and the CDP–Etn pathway, respectively. Dots represent the median value from four biologically independent replicates (two-tailed Student's t-test). Panel **a** created with BioRender.com.

synaptotagmin-like mitochondrial lipid-binding protein (SMP) domain, has also been reported to localize at the ER–mitochondria interface[36]. Our results demonstrated that PDZD8 contributes to lipid transport between the ER and mitochondria in HeLa cells. Specifically, the relative intensities of PL-^{13}C-PE(16:0_18:1) and PL-^{13}C-PE(18:1_18:1) were significantly decreased in *PDZD8* knock-down cells. However, the relative intensity of PL-^{13}C-PE(18:0_20:4) was not decreased in PDZD8 deficiency cells, suggesting that PDZD8 had fatty acid chain selectivity in lipid transport (Fig. 3j and Supplementary Fig. 8).

Contribution of the CDP–Etn pathway to mitochondrial PE pool

In eukaryotic cells, the CDP–ethanolamine (CDP–Etn) pathway contributes to the de novo PE biosynthesis in the ER (Fig. 4a). A previous report has revealed that part of the mitochondrial PE lipids may originate from the CDP–Etn biosynthesis pathway in ER[37]. However, little quantitative characterization of the PE lipid transport between the ER and mitochondria has occurred. To quantitatively explore the contribution of the CDP–Etn pathway to the mitochondrial PE lipid

pool, we conducted a continuous stable-isotope labelling experiment using [U-^{13}C]-Etn to label newly synthesized PE lipids in the ER ($^{13}C_2$-PE). Subsequently, we employed photocatalytic proximity labelling of PE lipids in mitochondria (Fig. 4a). The LC-MS analyses of dual-labelled PE lipids (PL-^{13}C-PE) in mitochondria enabled a quantitative characterization of that mitochondrial PE lipids that originated from the CDP–Etn pathway in the ER. A total of 18 dual-labelled PE lipids in HeLa cells were quantified (Fig. 4b). Among the 18 dual-labelled PE lipids analysed, PE(18:1_18:1) was the most abundant (38.5%), followed by PE(16:0_18:1), PE(18:0_18:1), PE(16:1_18:1) and PE(18:1_20:5), collectively composing 80.8% of the PE lipids transported from the ER to the mitochondria (Fig. 4c). To further validate the contribution of the CDP–Etn pathway in the ER to the PE pool in the mitochondria, we used the small molecule meclizine to inhibit PCYT2 enzyme in the pathway[38]. Consequently, the fractions of dual-labelled PE lipids significantly decreased in the mitochondria (Fig. 4d).

We applied the first-order exponential function to quantitatively fit the kinetics of the mitochondrial PE lipids derived from the CDP–Etn biosynthesis pathway (Fig. 4e,f and Supplementary Fig. 9). The turnover fractions of PL-^{13}C-PE(20:1_20:4) and PL-^{13}C-PE(18:1_18:1) from the CDP–Etn pathway were gradually increased to 0.11 and 0.34, respectively, in the mitochondria within 72 h (Fig. 4e,f). Integrated PSD and CDP–Etn pathways yielded combined fractions of 0.75 and 0.78 for these species, respectively (Fig. 4g,h). Here, to further validate the complementary contributions of the PSD and CDP–Etn pathways to mitochondrial PE lipids, we performed multi-labelling with both d_4-Etn and [U-^{13}C]-serine in one experiment. The results from simultaneous multi-tracer labelling showed good consistency with the cumulative results from individual tracer labelling (Extended Data Fig. 6g–i).

Overall, the PSD pathway accounted for 59.9% of mitochondrial PE lipids, while the CDP–Etn pathway contributed 19.2% (Fig. 4i and Extended Data Fig. 6a–f). The remaining 20.9% of the PE lipids may originate from other pathways, such as the acylation of LPE, or from the ^{12}C-serine from de novo synthesis and protein degradation. Notably, the transport preference of PE lipids from the ER to mitochondria was observed to be opposite that of the exchange route of PS from the ER to mitochondria. Mitochondrial PE lipids from the PSD pathway showed lower fractions containing C18:1 than those without, whereas the CDP–Etn pathway exhibited higher C18:1-containing fractions (Fig. 4j). The results perfectly illustrated the complementary roles of the two pathways contributing to the PE lipid pool in mitochondria.

Quantitative profiling of lipid turnover in nucleus

We extended our technology to characterize lipid turnover in the nucleus using nucleus-selective proximity labelling. HeLa cells were continuously labelled with [U-^{13}C]-Etn to trace newly synthesized PE lipids in the ER (Fig. 5a). Using AO as the photocatalyst, a total of 21 dual-labelled PE lipids in the nucleus were quantified by LC-MS (Fig. 5b). These lipids displayed distinct turnover kinetics, dependent on the fatty acyl chain composition. We further determined the relative percentages of PE lipids in the nucleus from the CDP–Etn pathway (Fig. 5c). PE(18:1_18:1), PE(16:0_18:1) and PE(18:0_18:1) were the major PE lipids biosynthesized in the ER and then transported to the nucleus, and they accounted for 69.3% of the ER-derived nuclear PE. Among them, PE(18:1_18:1) exhibited a high turnover fraction but a slower rate, indicating complex turnover dynamics in the nucleus (Fig. 5d and Supplementary Fig. 10). Finally, quantitative analysis revealed that 21 PE lipids biosynthesized in the ER contributed 52.2% to the total PE lipids present in the nucleus (Fig. 5e and Extended Data Fig. 7a–f).

We also profiled PS lipids using [U-^{13}C]-serine labelling, identifying ten dual-labelled PS lipids in the nucleus (Fig. 5f). Among them, PS(36:1), PS(16:0_18:1) and PS(36:2) contributed 81.3% of the total PS lipids that moved from the ER to the nucleus (Fig. 5g), with PS turnover rates significantly higher than those of PE (Fig. 5h,i and Supplementary Fig. 11). Further quantification revealed that ten PS lipids biosynthesized in the ER contributed 74.9% to the total PS lipids present in the nucleus (Fig. 5j and Extended Data Fig. 7g–l).

In the same [U-^{13}C]-serine labelling experiment, we also measured dual-labelled PE lipids (PL-^{13}C-PE) using nucleus-specific proximity labelling (Extended Data Fig. 8). Twenty-one PE lipids in the nucleus biosynthesized from the PSD pathway accounted for 34.1% of the total PE lipids present in the nucleus. Thus, the CDP–Etn pathway and the PSD pathway collectively accounted for 86.3% of the PE pool in the nucleus (Fig. 5k). The previous study revealed that PSD is predominantly located in mitochondria[18]. Additionally, turnover rates and maximum turnover fractions of four dominant PE lipids in the nucleus via the PSD pathway were considerably less than those in the mitochondria (Extended Data Fig. 8e). Collectively, the results suggested that PE lipids biosynthesized from the PSD pathway in the mitochondria also importantly contributed to the PE pool in the nucleus.

Photocatalytic labelling enables lysosomal lipid analysis

The lysosome, a key degradative organelle, plays a crucial role in cellular metabolism and signalling. Using a dual-labelling strategy, we quantitatively characterized the sources of 18 dual-labelled PE lipids in the lysosome and found that lysosomal PE lipids derived from the CDP–Etn pathway or the PSD pathway exhibited fatty acyl chain dependency (Fig. 6a and Extended Data Fig. 9a–d). The two pathways complementarily contributed to the lysosomal PE lipids (Extended Data Fig. 9e). Furthermore, we quantified the contribution percentage of each pathway to the PE pool in the lysosome. The CDP–Etn pathway contributed 60.8% of lysosomal PE lipids, while the PSD pathway accounted for 31.3% of lysosomal PE lipids (Fig. 6b). We further characterized the relative abundance of individual PE species that originated from the CDP–Etn pathway in the ER. Among them, PE(18:1_18:1), PE(16:0_18:1), PE(18:0_18:1) and PE(16:1_18:1) collectively accounted for 73.6% of the ER-derived PE in the lysosome (Fig. 6c). Similarly, the relative abundance of individual PE species via the PSD pathway was calculated. Among them, PE(18:0_18:1), PE(16:0_18:1), PE(18:0_20:4), PE(18:1_18:1) and PE(18:0_20:5) were the five major PSD-pathway-derived PE lipids in the lysosome, constituting 77.5% of the total PE lipids from this pathway (Fig. 6d).

mTOR is a serine/threonine protein kinase that regulates metabolic networks and cellular homeostasis by sensing environmental signals such as nutrients and growth factors[39]. Here we employed lysosome-specific photocatalytic labelling to characterize the impact of mTOR on lysosomal lipid metabolism. First we used the mTOR activator MHY1485 to treat mouse embryonic fibroblast (MEF) cells and conducted both whole-cell and lysosome-specific lipidomic analysis. A total of five lipid classes including cholesterol, PE, PS, plasmenyl PE (PE(P)) and LPE were detected in both whole cells and lysosomes. Principal component analysis revealed no distinct separation between the control and MHY1485-treatment groups. However, these lipid classes exhibited notable differences in the lysosome upon MHY1485 treatment, particularly in the first principal component (PC1) dimension (Fig. 6e). The effects of mTOR activation using MHY1485 on the abundance of different lipid classes were measured. Lysosomal abundances of cholesterol, PE, PS and PE(P) lipids significantly increased, whereas whole-cell levels remained unchanged (Fig. 6f). To further validate the association between lysosomal lipid accumulation and mTOR pathway activity, we treated cells with mTOR inhibitors rapamycin (Fig. 6g) or torin1 (Fig. 6h) following MHY1485-induced mTOR activation. The mTOR inhibition significantly reduced lysosomal cholesterol and glycerophospholipid levels, reversing the accumulation observed under MHY1485 treatment. Notably, inhibition of endocytosis with dynasore reduced lysosomal lipid accumulation during mTOR activation, suggesting that enhanced endocytic trafficking from the plasma membrane contributes to this phenotype. Supplementation with exogenous d_7-PE(15:0/18:1) further confirmed that the accumulated lysosomal lipids primarily originate from the internalized plasma membrane

https://doi.org/10.1038/s41557-025-01886-w

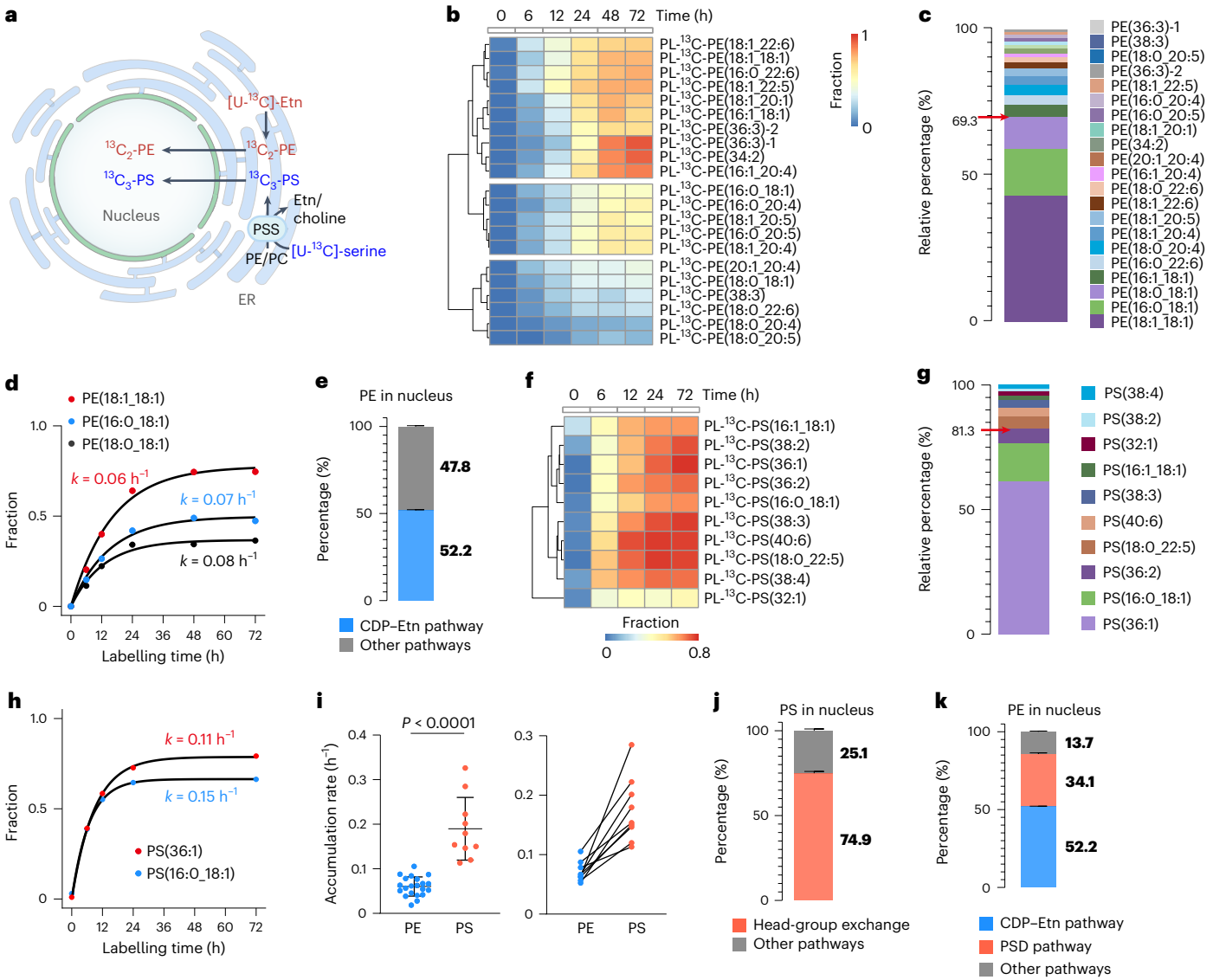

Fig. 5 | Quantitative profiling of lipid turnover in nucleus. a, Schematic illustration of PE and PS biosynthesis in the ER that is contributed to the nucleus. **b**, Hierarchical clustering analysis of 21 dual-labelled PE lipids (PL-^{13}C-PE) accumulated in the nucleus of HeLa cells. **c**, Relative percentages of newly synthesized PE lipids in the nucleus, biosynthesized from the CDP–Etn pathway in the ER. The red arrow indicates the relative percentage of three predominant PE lipids in nucleus biosynthesized from the CDP–Etn pathway. The '-1' and '-2' labels in **b** and **c** are used to distinguish lipid isomers that share the same annotation. **d**, The quantitative fit of the turnover kinetics of three newly synthesized PE lipids in the nucleus using the first-order exponential function. The dots represent the median value from four biologically independent replicates. **e**, The contribution percentage of the CDP–Etn pathway in the ER to the PE lipid pool in the nucleus. Bar plots represent median ± s.d. **f**, Hierarchical clustering analysis of ten dual-labelled PS lipids (PL-^{13}C-PS) accumulated in the nucleus of HeLa cells. **g**, Relative percentages of newly synthesized PS lipids in the nucleus, biosynthesized from the head-exchange reactions in the ER. The red arrow indicates the relative percentage of three predominant PS lipids in nucleus biosynthesized from the head-group exchange. **h**, The quantitative fit of the turnover kinetics of two newly synthesized PS lipids in the nucleus using the first-order exponential function. The dots represent the median value from four biologically independent replicates. **i**, Comparisons of turnover rates (k) between PE and PS lipids in the nucleus. The horizontal bars and error bars represent mean ± s.d. (two-tailed Student's t-test). **j**, The contribution percentage of PS biosynthesized in the ER to the PS lipid pool in the nucleus. **k**, Contribution percentages of two PE biosynthesis pathways to the PE lipid pool in the nucleus of HeLa cells. Bar plots represent median ± s.d. in **j** and **k**; $n = 4$ biologically independent replicates in **b**–**k**.

(Supplementary Fig. 12). These findings establish a direct functional link between mTOR activation and lysosomal lipid accumulation.

Discussion

We developed a photocatalytic proximity labelling strategy for organelle-selective lipid analysis in live cells by MS. This approach employed organelle-localized dyes to activate reactive species from labelling probes via visible light irradiation, enabling selective, biocompatible lipid labelling without organelle isolation. We applied the strategy to the quantitative profiling of lipid transport between organelles in live cells with both pulse-chase labelling and continuous labelling. While pulse-chase labelling elucidates lipid transport kinetics at the molecular level, continuous labelling quantifies lipid pool turnover within specific organelles at the population level. Most importantly, this approach enables quantification of the contributions of different biosynthesis pathways to organelle lipid compositions. Unlike other lipid labelling technologies, our technology enabled the profiling of lipid transport without modifying lipid structures that could potentially influence inter-organelle lipid transport and lipid metabolism. Notably, MS analysis allowed the characterization and

https://doi.org/10.1038/s41557-025-01886-w

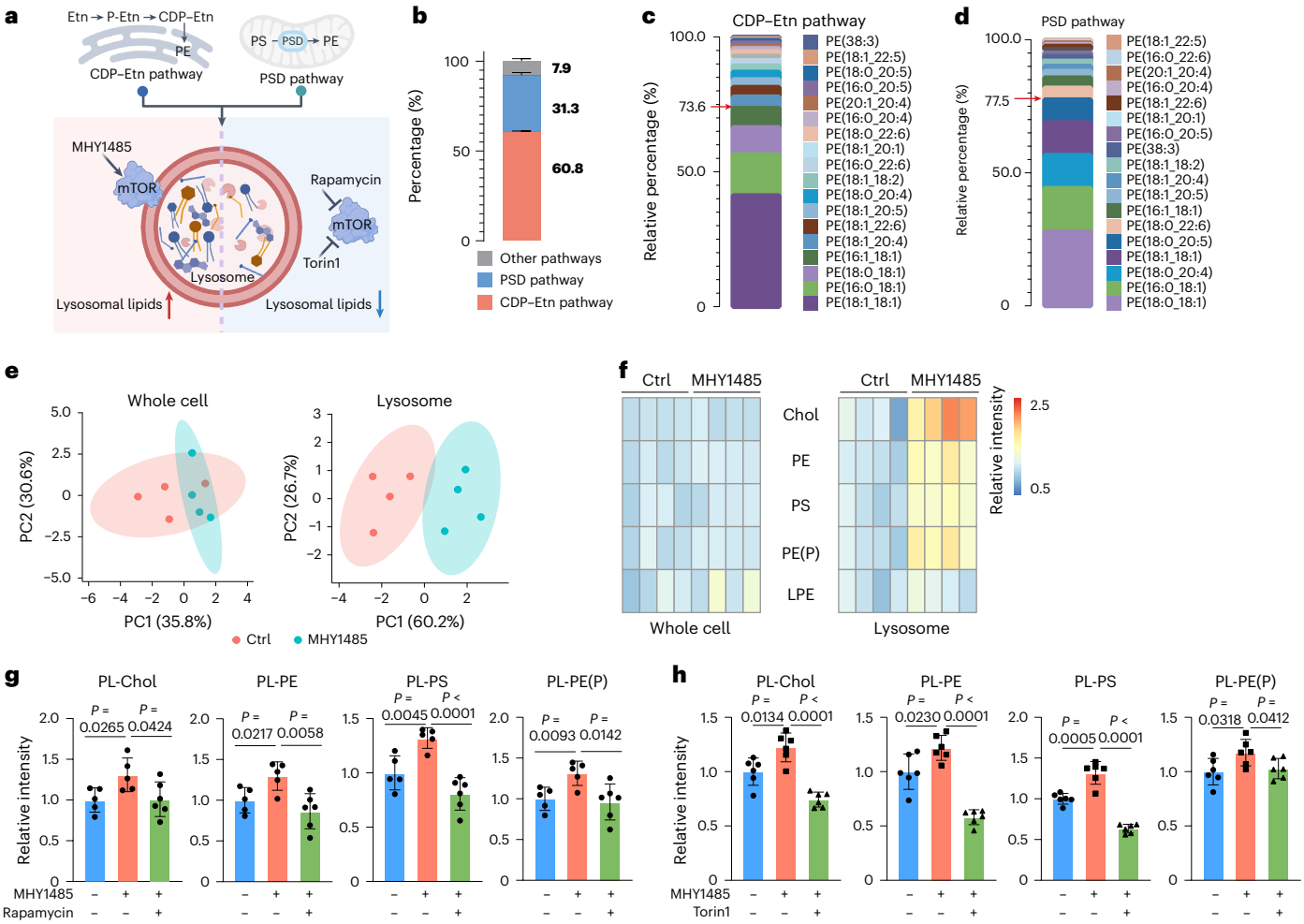

Fig. 6 | Quantitative characterization of PE lipid origin and metabolism in lysosomes. a, Schematic illustration of the origin of PE in lysosomes and lipid metabolism under mTOR activation or inhibition. **b**, Relative contributions of CDP–Etn and PSD pathways to the lysosomal PE lipid pool in HeLa cells. Bar plots represent mean ± s.d. ($n = 4$ biologically independent replicates for each pathway). **c**, Relative percentage of newly synthesized PE lipids in lysosomes produced via the CDP–Etn pathway within the ER. The red arrow indicates the relative percentage of four predominant PE lipids in lysosomes biosynthesized from the CDP–Etn pathway. **d**, Relative percentage of newly synthesized PE lipids in lysosomes from the PSD pathway in mitochondria. The red arrow indicates the relative percentage of five predominant PE lipids in lysosomes biosynthesized from the PSD pathway. **e**, Principal component analysis plot reveals minimal global lipidomic perturbations in MHY1485-treated cells (10 μM for 4 h) relative to the control (Ctrl), while demonstrating notable alterations in lysosomal lipid metabolism. **f**, Relative lipid class abundance from whole-cell lipidomic profiles and lysosome-specific PL lipids under vehicle control or MHY1485 treatment. **g**,**h**, Relative intensity of lysosome-specific PL lipid classes under MHY1485 treatment alone and in combination with rapamycin (**g**) or torin1 (**h**) treatment. Cells were treated with 10 μM MHY1485 and followed by rapamycin (100 nM) or torin1 (250 nM) for 12 h. Bar plots represent mean ± s.d.; $n = 5$ biologically independent samples for the control and MHY1485 groups in **g**; $n = 6$ biologically independent samples for the rapamycin group in **g** and for all groups in **h**; *P* values were calculated using two-tailed Student's *t*-test. Panel **a** created with BioRender.com.

comparison of fatty-acyl-dependent lipid transport, which cannot be readily achieved by fluorophore tagging. Quantitative kinetic characteristics of lipid transport between organelles, including turnover rate, maximum turnover fraction and turnover half-time ($t_{1/2}$), were obtained (Supplementary Figs. 6 and 9–11). This approach unveiled distinct biosynthesis pathways and transport routes contributing to lipid compositions in the mitochondria, nucleus and lysosomes.

We quantitatively profiled PE lipid turnover in the mitochondria, nucleus and lysosomes using dual-labelling and organelle-specific photocatalytic strategies. In mitochondria, the PSD pathway was the primary source of PE lipids (~60%), while the CDP–Etn pathway contributed ~20%, revealing their complementary roles to the mitochondrial PE lipid pool. Using dual labelling in LTP-deficient HeLa cells, we showed that VPS13A is critical for ER-to-mitochondria phospholipid transport, while PDZD8 selectively transfers lipids based on acyl chain composition. In the nucleus, the CDP–Etn pathway and PSD pathway contributed 52.2% and 34.1% of the PE lipids, respectively. We also quantified the kinetics of PS lipid turnover in the nucleus, which constituted about 75% of the total nuclear PS lipids. Remarkably, PS accumulates in the nucleus faster than PE, likely due to the quicker synthesis of PS via head-exchange reactions. Although AO enabled nuclear lipid labelling, its potential off-targeting of other acidic organelles[40] highlights the need for more nucleus-specific catalytic dyes. Notably, given the continuity between the ER and outer nuclear membrane, lipid transport to the nucleus may occur via lateral diffusion. Since AO localizes to the nucleus by binding to nucleic acids and the aryl azide probe has limited diffusion[41], most labelled lipids likely originate from the inner nuclear membrane. However, due to the limited spatial resolution, distinguishing between inner and outer nuclear membranes remains challenging. Future work using HaloTag-tagging of inner and outer nuclear membrane proteins to anchor photosensitizers may enable more precise spatial mapping of nuclear lipid dynamics. In lysosomes, the CDP–Etn pathway and PSD pathway contributed 60.8% and 31.3% of lysosomal PE lipids, respectively. Notably, mTOR activation selectively increased

lysosomal levels of cholesterol, PE and PS without altering global lipid profiles. This effect was reversed by mTOR inhibitors, underscoring its role in lysosomal lipid regulation. Together, photocatalytic proximity labelling of lipids provides a framework for quantitatively studying lipid transport and turnover at a subcellular resolution, providing insights into the dynamic landscape of lipid homeostasis in live cells.

While our photocatalytic proximity labelling strategy for lipids offers notable advantages, several aspects remain open for further optimization and development. First, we employed aryl azide as the reactive moiety in our probes, which preferentially reacts with lipids containing nucleophilic head groups. This approach enabled the generation of more interpretable MS/MS spectra, facilitating structural analysis of the PL lipids. To expand lipid coverage, alternative photocatalytic probes such as diazirines and phenols—commonly used in protein labelling—could be adapted for lipid labelling[41]. Although this study focused on PE and PS turnover, the development of new probes for other lipid classes and organelle-specific photocatalysts could broaden applicability. Second, the subcellular specificity of our method relied on the targeted localization of photosensitizers, which we achieve by screening commercially available subcellular dyes. These dyes are widely accessible and practical. Moreover, one can also conjugate photosensitizers with targeting units such as antibodies or small-molecule ligands to enable spatial restriction. For instance, antibody-conjugated photosensitizers can selectively label cell surface proteins[25], while ligand-targeted dyes[22,42] can pinpoint intracellular compartments like the nucleus and lysosomes. These modular approaches not only advance proximity labelling of proteins but also could pave the way for organelle-specific proximity-labelled lipid analysis. Third, our method quantifies lipid turnover between donor and acceptor organelles under steady-state conditions, reflecting the net outcome of biosynthesis and intracellular distribution. However, it does not resolve specific transport routes, such as direct inter-organelle lipid transfer or multistep vesicular trafficking. To address this limitation, photocatalytic proximity labelling can be combined with pathway-specific inhibition or genetic perturbations to selectively block or modulate trafficking pathways, enabling more precise dissection of the lipid transport dynamics at the organelle level.

Online content

Any methods, additional references, Nature Portfolio reporting summaries, source data, extended data, supplementary information, acknowledgements, peer review information; details of author contributions and competing interests; and statements of data and code availability are available at https://doi.org/10.1038/s41557-025-01886-w.

References

1. Van Meer, G., Voelker, D. R. & Feigenson, G. W. Membrane lipids: where they are and how they behave. *Nat. Rev. Mol. Cell Biol.* **9**, 112–124 (2008).
2. Harayama, T. & Riezman, H. Understanding the diversity of membrane lipid composition. *Nat. Rev. Mol. Cell Biol.* **19**, 281–296 (2018).
3. Han, X. Lipidomics for studying metabolism. *Nat. Rev. Endocrinol.* **12**, 668–679 (2016).
4. Bar-Peled, L. & Kory, N. Principles and functions of metabolic compartmentalization. *Nat. Metab.* **4**, 1232–1244 (2022).
5. Sarmento, M. J. et al. The expanding organelle lipidomes: current knowledge and challenges. *Cell. Mol. Life Sci.* **80**, 237 (2023).
6. Vance, J. E. Phospholipid synthesis and transport in mammalian cells. *Traffic* **16**, 1–18 (2015).
7. Wong, L. H., Gatta, A. T. & Levine, T. P. Lipid transfer proteins: the lipid commute via shuttles, bridges and tubes. *Nat. Rev. Mol. Cell Biol.* **20**, 85–101 (2019).
8. Kaplan, M. R. & Simoni, R. D. Intracellular transport of phosphatidylcholine to the plasma membrane. *J. Cell Biol.* **101**, 441–445 (1985).
9. Shiao, Y. J., Lupo, G. & Vance, J. E. Evidence that phosphatidylserine is imported into mitochondria via a mitochondria-associated membrane and that the majority of mitochondrial phosphatidylethanolamine is derived from decarboxylation of phosphatidylserine. *J. Biol. Chem.* **270**, 11190–11198 (1995).
10. Feng, S. et al. Mitochondria-specific photoactivation to monitor local sphingosine metabolism and function. *eLife* **7**, e34555 (2018).
11. Feng, S. et al. Lysosome-targeted photoactivation reveals local sphingosine metabolism signatures. *Chem. Sci.* **10**, 2253–2258 (2019).
12. Rudd, A. K., Mittal, N., Lim, E. W., Metallo, C. M. & Devaraj, N. K. A small molecule fluorogenic probe for the detection of sphingosine in living cells. *J. Am. Chem. Soc.* **142**, 17887–17891 (2020).
13. Tamura, T. et al. Organelle membrane-specific chemical labeling and dynamic imaging in living cells. *Nat. Chem. Biol.* **16**, 1361–1367 (2020).
14. Thiele, C., Wunderling, K. & Leyendecker, P. Multiplexed and single cell tracing of lipid metabolism. *Nat. Methods* **16**, 1123–1130 (2019).
15. John Peter, A. T., Petrungaro, C., Peter, M. & Kornmann, B. METALIC reveals interorganelle lipid flux in live cells by enzymatic mass tagging. *Nat. Cell Biol.* **24**, 996–1004 (2022).
16. Qin, W., Cho, K. F., Cavanagh, P. E. & Ting, A. Y. Deciphering molecular interactions by proximity labeling. *Nat. Methods* **18**, 133–143 (2021).
17. Kang, M. G. & Rhee, H. W. Molecular spatiomics by proximity labeling. *Acc. Chem. Res.* **55**, 1411–1422 (2022).
18. Liu, Y. et al. Proximity chemistry in living systems. *CCS Chem.* **5**, 802–813 (2023).
19. Roux, K. J., Kim, D. I., Raida, M. & Burke, B. A promiscuous biotin ligase fusion protein identifies proximal and interacting proteins in mammalian cells. *J. Cell Biol.* **196**, 801–810 (2012).
20. Fang, Y. & Zou, P. Photocatalytic proximity labeling for profiling the subcellular organization of biomolecules. *ChemBioChem* **24**, e202200745 (2023).
21. Zhang, Y., Tan, J. & Chen, Y. Visible-light-induced protein labeling in live cells with aryl azides. *Chem. Commun.* **59**, 2413–2420 (2023).
22. Tamura, T., Takato, M., Shiono, K. & Hamachi, I. Development of a photoactivatable proximity labeling method for the identification of nuclear proteins. *Chem. Lett.* **49**, 145–148 (2020).
23. Wang, H. et al. Selective mitochondrial protein labeling enabled by biocompatible photocatalytic reactions inside live cells. *JACS Au* **1**, 1066–1075 (2021).
24. Oslund, R. C. et al. Detection of cell–cell interactions via photocatalytic cell tagging. *Nat. Chem. Biol.* **18**, 850–858 (2022).
25. Geri, J. B. et al. Microenvironment mapping via Dexter energy transfer on immune cells. *Science* **367**, 1091–1097 (2020).
26. Huang, Z. et al. Bioorthogonal photocatalytic decaging-enabled mitochondrial proteomics. *J. Am. Chem. Soc.* **143**, 18714–18720 (2021).
27. Tay, N. E. S. et al. Targeted activation in localized protein environments via deep red photoredox catalysis. *Nat. Chem.* **15**, 101–109 (2023).
28. Baracca, A., Sgarbi, G., Solaini, G. & Lenaz, G. Rhodamine 123 as a probe of mitochondrial membrane potential: evaluation of proton flux through F_0 during ATP synthesis. *Biochim. Biophys. Acta* **1606**, 137–146 (2003).
29. Karaj, E., Sindi, S. H. & Tillekeratne, L. V. Photoaffinity labeling and bioorthogonal ligation: two critical tools for designing "fish hooks" to scout for target proteins. *Bioorg. Med. Chem.* **62**, 116721 (2022).
30. Hoshi, K., Katayose, H., Yanagida, K., Kimura, Y. & Sato, A. The relationship between acridine orange fluorescence of sperm nuclei and the fertilizing ability of human sperm. *Fertil. Steril.* **66**, 634–639 (1996).
31. Zhu, H. et al. Metabolomic profiling of single enlarged lysosomes. *Nat. Methods* **18**, 788–798 (2021).

32. Bellance, N. et al. Doxorubicin inhibits phosphatidylserine decarboxylase and modifies mitochondrial membrane composition in HeLa cells. *Int. J. Mol. Sci.* **21**, 1317 (2020).
33. Calzada, E., Onguka, O. & Claypool, S. M. Phosphatidylethanolamine metabolism in health and disease. *Int. Rev. Cell Mol. Biol.* **321**, 29–88 (2016).
34. Yaffe, M. P. & Kennedy, E. P. Intracellular phospholipid movement and the role of phospholipid transfer proteins in animal cells. *Biochemistry* **22**, 1497–1507 (1983).
35. Kumar, N. et al. VPS13A and VPS13C are lipid transport proteins differentially localized at ER contact sites. *J. Cell Biol.* **217**, 3625–3639 (2018).
36. Hirabayashi, Y. et al. ER-mitochondria tethering by PDZD8 regulates Ca^{2+} dynamics in mammalian neurons. *Science* **358**, 623–630 (2017).
37. Camici, O. & Corazzi, L. Import of phosphatidylethanolamine for the assembly of rat brain mitochondrial membranes. *J. Membr. Biol.* **148**, 169–176 (1995).
38. Gohil, V. M. et al. Meclizine inhibits mitochondrial respiration through direct targeting of cytosolic phosphoethanolamine metabolism. *J. Biol. Chem.* **288**, 35387–35395 (2013).
39. Saxton, R. A. & Sabatini, D. M. mTOR signaling in growth, metabolism, and disease. *Cell* **168**, 960–976 (2017).
40. Krolenko, S. A., Adamyan, S. Y., Belyaeva, T. N. & Mozhenok, T. P. Acridine orange accumulation in acid organelles of normal and vacuolated frog skeletal muscle fibres. *Cell Biol. Int.* **30**, 933–939 (2006).
41. Lin, Z. et al. Multiscale photocatalytic proximity labeling reveals cell surface neighbors on and between cells. *Science* **385**, eadl5763 (2024).
42. Zhang, Y. et al. In situ lysosomal proteomics enabled by bioorthogonal photocatalytic proximity labelling. *Nat. Catal.* **8**, 162–177 (2025).

Publisher's note Springer Nature remains neutral with regard to jurisdictional claims in published maps and institutional affiliations.

Springer Nature or its licensor (e.g. a society or other partner) holds exclusive rights to this article under a publishing agreement with the author(s) or other rightsholder(s); author self-archiving of the accepted manuscript version of this article is solely governed by the terms of such publishing agreement and applicable law.

© The Author(s), under exclusive licence to Springer Nature Limited 2025

Methods

Chemicals

LC-MS-grade water (H_2O), methanol (MeOH), isopropyl alcohol (IPA) and HPLC-grade dichloromethane (DCM) were purchased from Honeywell. LC-MS-grade acetonitrile (ACN) and HPLC-grade methyl-*tert*-butyl ether (MTBE) were purchased from Merck. All lipid standards were purchased from Avanti Polar Lipids and Sigma-Aldrich. Lipid standards were dissolved in either MeOH or chloroform depending on the polarity and solubility. The [U-^{13}C]-serine was purchased from Cambridge Isotopes Laboratories. The [U-^{13}C]-Etn was purchased from Sigma-Aldrich.

Preparation of liposomes

The preparation of lipidomes follows a previous publication[12]. Briefly, 200 nmol of each individual lipid standard dissolved in MeOH was mixed with 5 µmol DOPC (157.2 µl of 25 mg ml^{-1} stock solution in $CHCl_3$) and dried by nitrogen gas. Then, 1 ml PBS was added into the dried lipid mixture. The solution was tumbled at room temperature for 1 h. After tumbling, the formed solution was subjected to ten freeze–thaw cycles using a dry ice and ethanol bath and a water bath (37 °C) with vortexing before every freeze step. The solution was then extruded 21 times through a 100 nm polycarbonate filter (Whatman, GE Healthcare Bio-Sciences) using an Avanti Mini-Extruder (Avanti Polar Lipids) to generate the liposome solution. Finally, 50 µl of liposome solution was taken for photocatalytic labelling of lipids in vitro, which contained 10 nmol of each individual lipid standard.

Photocatalytic labelling of lipids in vitro

The AzPh–alkyl–TA probe (100 nmol; 25 mM stock solution in DMSO) and the organic dye (AO, Rh 123 and fluorescein; 10 nmol each; 50 mM stock solution in DMSO) was sequentially added into a liposome solution (50 µl) prepared as previously described. Then, PBS was added, keeping the total solution volume to 100 µl. The solution was mixed and irradiated at 25 °C with blue light-emitting diode (LED) irradiation (BioBlue 058B; Shanghai Qiding; wavelength, 468 nm; 4 W) for 60 min. After that, the solution was transferred to a new Eppendorf tube for lipid extraction.

Photocatalytic proximity labelling of lipids in live cells

The HeLa cell line and MEF cell line used in this study were obtained from American Type Culture Collection. Cells were seeded in 10 cm cell culture plates with Dulbecco's Modified Eagle Medium (DMEM) containing 10% foetal bovine serum (FBS) and antibiotics (penicillin at 100 U ml^{-1} and streptomycin at 100 µg ml^{-1}). At ~80% confluence, the organic dye (4 µl of 50 mM Rh 123; 2 µl of 50 mM AO; 10 µl of 2 mM DND-189) was added to the medium and incubated for 20 min (for cells incubated with Rh 123 and AO) or 5 min (for cells incubated with DND-189). Then, the culture medium was removed. Cells were washed twice with PBS. The medium was replaced by fresh DMEM without phenol red and containing 200 µM AzPh–alkyl–TA probe (for cells incubated with Rh 123), 100 µM AzPh–alkyl–TA probe (for cells incubated with AO) or 50 µM AzPh–alkyl–TA probe (for cells incubated with DND-189). Cells were further incubated for 30 min (for cells incubated with Rh 123 and AO) or 5 min (for cells incubated with DND-189), followed by blue light irradiation for 60 min (for cells incubated with Rh 123 and AO) or 15 min (for cells incubated with DND-189). After that, cells were washed again with PBS. Finally, cells were quickly scraped and collected by centrifuge for 2 min at 800*g* and 4 °C for lipid extraction.

Pulse-chase labelling and photocatalytic proximity labelling

For pulse-chase labelling, HeLa cells were seeded in 10 cm cell culture plates with DMEM containing 10% dialysed FBS (dFBS) and antibiotics (penicillin at 100 U ml^{-1} and streptomycin at 100 µg ml^{-1}). HeLa cells were first cultured for 16 h. Then, the culture medium was replaced with serine-free DMEM containing 0.4 mM [U-^{13}C]-serine and 10% dFBS. Cells were further cultured for 24 h. Then, cells were washed with PBS and chased in unlabelled culture medium containing 2.0 mM serine for 15, 30, 45, 60, 90 or 120 min. After that, the photocatalytic proximity labelling reaction was performed. Some 2 µl of 50 mM Rh 123 was added at 5, 20, 35, 50, 80 and 110 min during the chasing time and incubated for 10 min. Then, the culture medium was removed. Cells were washed twice with PBS. The medium was replaced by fresh DMEM without phenol red and containing 100 µM AzPh–alkyl–TA probe. Cells were further incubated 5 min, followed by blue light irradiation for 15 min. After that, cells were washed again with PBS. Finally, cells were quickly scraped and collected by centrifuge for 2 min at 800*g* and 4 °C for lipid extraction.

Continuous labelling and photocatalytic proximity labelling

For continuous stable-isotope labelling, HeLa cells were seeded in 10 cm cell culture plates with DMEM containing 0.4 mM Etn, 10% dFBS and antibiotics (penicillin at 100 U ml^{-1} and streptomycin at 100 µg ml^{-1}). HeLa cells were first cultured for 16 h. Then, the culture medium was replaced with Etn-free DMEM containing 0.4 mM [U-^{13}C]-Etn and 10% dFBS or serine-free DMEM containing 0.4 mM [U-^{13}C]-serine and 10% dFBS. The stable-isotope labelling took 6 h, 12 h, 24 h, 48 h or 72 h as indicated. After that, the photocatalytic proximity labelling reaction was performed as previously described. For samples with a labelling time of 0 h, after a 16 h culture, the culture medium was replaced with Etn-free DMEM containing 0.4 mM [U-^{13}C]-Etn (or serine-free DMEM containing 0.4 mM [U-^{13}C]-serine), 10% dFBS and the organic dye (4 µl of 50 mM Rh 123, 2 µl of 50 mM AO or 10 µl of 2 mM DND-189). After that, the photocatalytic proximity labelling reaction was performed as previously described.

Lipid extraction

The lipids were extracted with a modified MTBE protocol that followed our previous publications[43,44]. For photocatalytic labelling of lipids in liposomes, the reaction solution was first diluted to 400 µl with water. Then, 960 µl of the extraction solvent (MTBE/MeOH = 5:1, v/v) was added. The sample was vortexed for 60 s, followed by 10 min of sonication in a water bath (4 °C). The solution was centrifuged at 845*g* for 15 min at 4 °C. The upper organic layer (550 µl) was collected into a new Eppendorf tube. Then, 550 µl of MTBE was added to the remaining layer for further extraction. The solution was vortexed, sonicated and centrifuged again. Then, the upper organic layer was collected. The re-extraction process was repeated three times in total to ensure a high extraction efficiency and recovery rate. Finally, the pooled organic layer was evaporated with a Labconco vacuum concentrator. The dry extract was reconstituted using 100 µl of DCM/MeOH (1:1, v/v) before LC-MS analysis. For lipid extraction of cell samples, cell pellets were first mixed with water (400 µl), vortexed for 60 s and incubated in liquid nitrogen for 1 min. Then, the mixture was thawed at room temperature and sonicated for 10 min. This freeze–thaw cycle was repeated three times in total. Then, 960 µl of the extraction solvent (MTBE/MeOH = 5:1, v/v) was added. The sample was vortexed for 60 s, followed by 10 min of sonication. The rest of the procedures were the same as those for lipid extraction of the liposome samples.

LC-MS/MS analysis

All lipidomics analyses were performed using an ultra HPLC system (1290 series, Agilent Technologies) coupled to a quadruple time-of-flight mass spectrometer (TripleTOF 6600, Sciex) or a mass spectrometer (timsTOF Pro, Bruker Daltonics) following the protocol in our previous publications[44,45]. Lipid separation was performed on a Phenomenex Kinetex C18 column (particle size, 1.7 µm; 100 mm (length) × 2.1 mm (inner diameter)) at 55 °C. Mobile phase A was H_2O/ACN (6:4, v/v) with 10 mM $HCOONH_4$, and mobile phase B was IPA/ACN (9:1, v/v) with 10 mM $HCOONH_4$. Lipids were eluted at 0.3 ml min^{-1} with a linear gradient of 40% B (0–1.5 min), 40% B to 85% B (1.5–10.5 min),

85% B (hold 10.5–14.0 min), 85% B to 100% B (14.0–14.1 min) and 100% B (hold 14.1–15.0 min), followed by a decrease to 40% B within 0.2 min and holding at 40% B for 2.8 min to reach column equilibrium.

The parameters for the Sciex TripleTOF 6600 were set as follows: ion source gas 1, 60 psi; ion source gas 2, 60 psi; curtain gas, 30 psi; temperature, 600 °C; ion spray voltage floating, 5,000 V in positive mode; and declustering potential, 100 V. A data-dependent acquisition (DDA) method was used for MS/MS acquisition. Each acquisition cycle consists of one rapid time-of-flight MS survey scan (200 ms) followed by the consecutive acquisition of 11 product ion scans (50 ms each). For the time-of-flight MS survey scan, the mass range is from 200 to 2,000 Da, and the collision energy is set to 10 V. For the product ion scan, the mass ranges are from 100 to 2,000 Da, and the collision energy is set to 45 ± 25 V. Dynamic background subtraction was applied. The dynamic exclusion was set to 4 s after two occurrences to ensure the non-repetitive acquisition of MS/MS spectra from the same ion. All analyses were performed in positive ion mode. The sample injection volume was 2 µl. The data were acquired using Analyst TF software (v.1.7.1, Sciex).

For data acquisition using the Bruker timsTOF Pro, PASEF-DDA scan mode was used. The parameters were set as follows: capillary voltages were +4,500 V for positive ionization mode; nebulizer pressure, 2.2 bar; dry gas, 10.0 l min^{-1}; dry temperature, 220 °C; number of PASEF MS/MS scans, 2; ramping time, 100 ms; total cycle time, 0.32 s; charge range, 1–2; absolute threshold, 100 counts; active exclusion was checked, and the former target ions were released after 0.1 min; isolation window, 1.2 Da; and collision energy, 40 eV. All analyses were performed in positive ion mode. The sample injection volume was 2 µl. The data were acquired using Bruker Compass HyStar (v.6.0.30.0, Bruker Daltonics).

Data processing

For data acquired using the Sciex TripleTOF 6600, raw MS data files (.wiff) were converted to .mzXML format using ProteoWizard (v.3.0.6428). Then, .mzXML data files were grouped for peak detection and alignment using the R package xcms (v.1.46.0). Detailed parameters followed those of our previous publication[45]. The generated MS1 peak table and MS/MS data file were used for the identification of PL lipids. First we curated an in-house library that contained the exact mass and MS/MS spectra of 1,164 PL lipids covering LPE, plasmenyl LPE (LPE(P)), plasmanyl LPE (LPE(O)), PE, PE(P), plasmanyl PE (PE(O)), LPS, PS, cholesterol and Sph at lipid species level with adduct form as $[M + 2H]^{2+}$. Identification of PL lipid was performed by MS1 match and MS/MS spectral match with the theoretical library by an R script. MS1 match tolerance was set as 15 ppm. For the MS/MS spectral match, the characteristic skeleton ions such as [(PL-PE/LPE) − (AzPh−alkyl−TA) − $C_2H_8NO_4P + H]^+$, [(PL-PS/LPS) − (AzPh−alkyl−TA) − $C_3H_8NO_6P + H]^+$ and [(PL-Sph/Chol) − (AzPh−alkyl−TA) − $C_2H_9NO + H]^+$ were used to match against that in the library. Finally, we performed a manual check to assure the identifications.

For dual-labelled PE and PS lipids, the Skyline software (v.22.2.0.351) was used for data analysis at the MS1 level. Raw data files (.wiff) and the isotopologue target list containing exact masses and retention times of precursor ions were imported into Skyline for targeted extraction. For each isotopologue, the integration range was manually checked and adjusted for accurate quantification. The quantification result was corrected with R package 'Accucor' (v.0.2.4) in MetTracer[46] for natural isotope correction. The corrected intensities of M0 represent unlabelled PL lipids (PL-^{12}C-lipid), while the corrected sum intensities of M1–M3 represent labelled PL lipids (PL-^{13}C-lipid) that are newly biosynthesized in the specific pathway. Then, the turnover fraction was calculated as equation (1):

$$\text{Fraction} = \frac{I_{\text{PL}-^{13}\text{C}-\text{lipid}}}{I_{\text{PL}-^{12}\text{C}-\text{lipid}} + I_{\text{PL}-^{13}\text{C}-\text{lipid}}} \quad (1)$$

where $I_{\text{PL}-^{13}\text{C}-\text{lipid}}$ and $I_{\text{PL}-^{12}\text{C}-\text{lipid}}$ represent the intensities of each labelled PL lipid (PL-^{13}C-lipid) and unlabelled PL lipid (PL-^{12}C-lipid), respectively. The first-order exponential function (equation (2)) was used to quantitatively fit the dynamic turnover of newly synthesized PE or PS lipids in mitochondria or the nucleus. Specifically, labelling fractions for each PL lipid at all time points were used to fit the exponential function using the nls function in the R package called stats (v.3.6.1).

$$\text{Fraction} = a - a \times e^{(-kt)} \quad (2)$$

where k is the first-order rate constant, representing the turnover rate; a is the maximum turnover fraction; and t is the labelling time in the continuous stable-isotope labelling experiment. Additionally, the turnover half-time $t_{1/2}$ could be calculated as $0.693/k$, indicating the half-time required to reach the maximum turnover fraction.

Photocatalytic proximity labelling of LTP-deficient HeLa cells

For small interfering RNA (siRNA) transfections, HeLa cells were transfected with 100 nM siRNA using Lipo2000 (Invitrogen) for 48 h following the manufacturer's instructions. The following sense sequences of siRNA were used: human *VPS13A*, 5′-GGAUAGAGCUUAUGAUUCA-3′; and human *PDZD8*, 5′-CCCAGUUCUUCCUGCUGUA-3′. After that, the culture medium was replaced with serine-free DMEM containing 0.4 mM [U-^{13}C]-serine and 10% dFBS. The stable-isotope labelling took 4 h. Then, the photocatalytic proximity labelling reaction was performed as previously described.

Cell viability analysis

HeLa cells had photocatalytic labelling performed with Rh 123 or DND-189 as the photocatalyst, as previously described. After cell collection (~5×10^6 cells per sample), 1 ml of medium was added to resuspend the cells. Then, 10 µl of cell suspension was taken to 190 µl with PBS in a new tube, followed by gently mixing with a pipette. Some 20 µl of 0.4% Trypan Blue solution (Thermo Fisher Scientific) was added to the diluted cell suspension. The cell suspension was gently mixed and then stood for 5 min at room temperature. Finally, 20 µl of cell suspension was applied to the cell counting plate (Countstar O010101) for automated analysis by a Countstar Easy Automated Cell Counter (RuiYu Biotech).

Hoechst 33342 and propidium iodide double staining was used for the cell viability evaluation of the nucleus-specific photocatalytic labelling. Briefly, HeLa cells were cultured in a 24-well plate, and we performed photocatalytic labelling with AO, as previously described. Then, cells were washed with 300 µl PBS. Some 1 ml DMEM without phenol red and containing 1 µg of propidium iodide and 5 nmol of Hoechst 33342 (Thermo Fisher Scientific) was added to each well. Finally, images were taken using a Leica DMi8 microscope. ImageJ was used for cell counting. The cell viability rate was calculated as equation (3):

$$\text{Cell viability} = 1 - \frac{N_{\text{PI}}}{N_{\text{Hoechst}}} \quad (3)$$

where N_{PI} and N_{Hoechst} represent the cell number with propidium iodide staining and the cell number with Hoechst 33342 staining, respectively.

Organic synthesis of labelling probes

All labelling probe synthesis procedures are provided in the Supplementary Information. Commercially available reagents were used without further purification. Thin layer chromatography was performed using Jiangyou thin layer chromatography silica gel plates HSG F254 and visualized using UV light and potassium permanganate. Flash chromatography was performed on a Lisure Science EZ purification system using the Santai Technologies silica gel cartridge. The ^{1}H and ^{13}C NMR spectra were recorded on an Agilent 500 MHz or an Agilent 600 MHz

spectrometer. Chemical shifts in ^{1}H NMR spectra were reported in parts per million on the δ scale from an internal standard of residual $CDCl_3$ (7.26 ppm) or CD_3OD (3.31 ppm). Data for ^{1}H NMR were reported as follows: chemical shift, multiplicity (s = singlet, d = doublet, t = triplet, q = quartet, dd = doublet of doublets, ddd = doublet of double doublets, m = multiplet, br = broad), coupling constant in hertz and integration. Data for ^{13}C NMR spectra were reported in terms of chemical shift in parts per million from the central peak of $CDCl_3$ (77.16 ppm) or CD_3OD (49.00 ppm). MS experiments were performed on a Bruker maXis 4G instrument for high-resolution MS electrospray ionization. NMR spectra are provided in Supplementary Fig. 13.

Statistics and reproducibility

Fluorescence imaging reported in Fig. 2b,d,f and Extended Data Fig. 3d was presented by observing at least 20 cells from five independent experiments, and selected representative data are shown. Fluorescence imaging reported in Extended Data Fig. 3c was presented by observing at least 20 cells from three independent experiments, and selected representative data are shown.

Reporting summary

Further information on research design is available in the Nature Portfolio Reporting Summary linked to this article.

Data availability

Unless otherwise stated, all data supporting the results of this study can be found in the article and Supplementary Information. The raw LC-MS data files generated in this study have been deposited in the National Omics Data Encyclopedia under accession code OEP00004920. Source data are provided with this paper.

References

43. Chen, X., Yin, Y., Zhou, Z., Li, T. & Zhu, Z. J. Development of a combined strategy for accurate lipid structural identification and quantification in ion-mobility mass spectrometry based untargeted lipidomics. *Anal. Chim. Acta* **1136**, 115–124 (2020).
44. Chen, X. et al. Trapped ion mobility spectrometry-mass spectrometry improves the coverage and accuracy of four-dimensional untargeted lipidomics. *Anal. Chim. Acta* **1210**, 339886 (2022).
45. Tu, J., Yin, Y., Xu, M., Wang, R. & Zhu, Z. J. Absolute quantitative lipidomics reveals lipidome-wide alterations in aging brain. *Metabolomics* **14**, 5 (2017).
46. Wang, R. et al. Global stable-isotope tracing metabolomics reveals system-wide metabolic alternations in aging *Drosophila*. *Nat. Commun.* **13**, 3518 (2022).

Acknowledgements

The work was supported by the National Natural Science Foundation of China (22425404 and 92357308 to Z.-J.Z. and 22337005 to Y.C.), Strategic Priority Research Program of the Chinese Academy of Sciences (XDB1060000 to Y.C.), Science and Technology Commission of Shanghai Municipality (21JC1405902 to Z.-J.Z.), Shanghai Key Laboratory of Aging Studies (19DZ2260400), Shanghai Municipal Science and Technology Major Project, Shanghai Basic Research Pioneer Project and Shanghai Post-doctoral Excellence Program (to X.C.). We thank C. Xu and Z. Cheng (Shanghai Institute of Biochemistry and Cell Biology, China) for kindly providing the *PISD* KO HeLa cells. Images in Figs. 1a, 2g,h, 3a,d,e,i, 4a and 6a were created with BioRender.com.

Author contributions

Z.-J.Z., Y.C. and X.C. conceived the idea and designed the experiments. X.C. and H.X. performed most experiments, including sample preparation, data acquisition, data processing and data analysis. R.H. synthesized labelling probes and performed microscopy experiments. R.W. contributed to the stable-isotope labelling experiment. Y.Y. contributed to the data analysis. Z.-J.Z. and Y.C. supervised the project. Z.-J.Z. and X.C. wrote the paper. All authors edited the paper.

Competing interests

The authors declare no competing interests.

Additional information

Extended data is available for this paper at https://doi.org/10.1038/s41557-025-01886-w.

Supplementary information The online version contains supplementary material available at https://doi.org/10.1038/s41557-025-01886-w.

Correspondence and requests for materials should be addressed to Yiyun Chen or Zheng-Jiang Zhu.

Peer review information *Nature Chemistry* thanks Christoph Thiele and the other, anonymous, reviewer(s) for their contribution to the peer review of this work.

Reprints and permissions information is available at www.nature.com/reprints.

https://doi.org/10.1038/s41557-025-01886-w

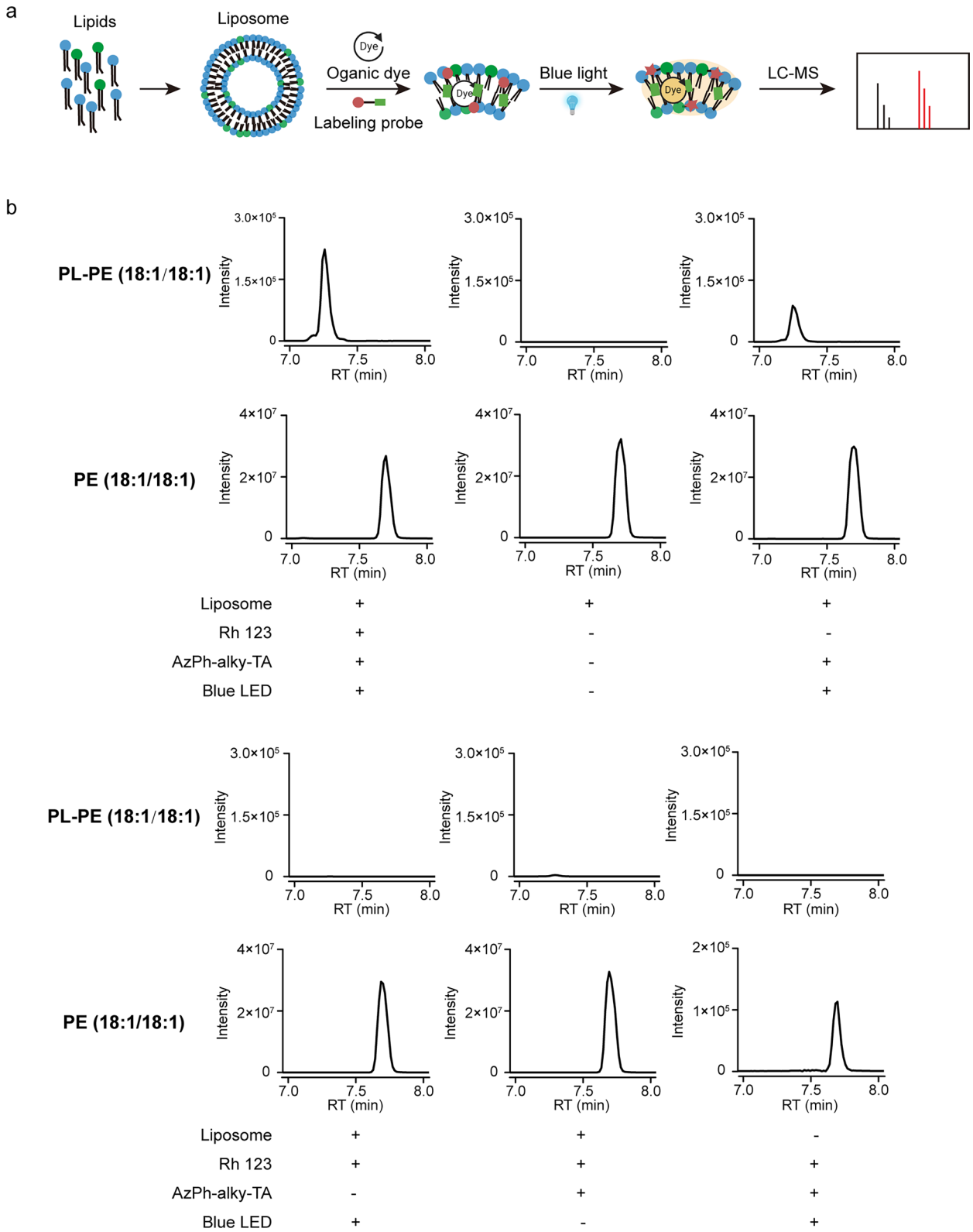

Extended Data Fig. 1 | Photocatalytic labeling of lipids under different conditions in vitro. (**a**) The characterization of the photocatalytic labeling of lipids in liposomes by LC-MS. (**b**) Intensity of PL-PE(18:1/18:1) and PE(18:1/18:1) under different conditions.

https://doi.org/10.1038/s41557-025-01886-w

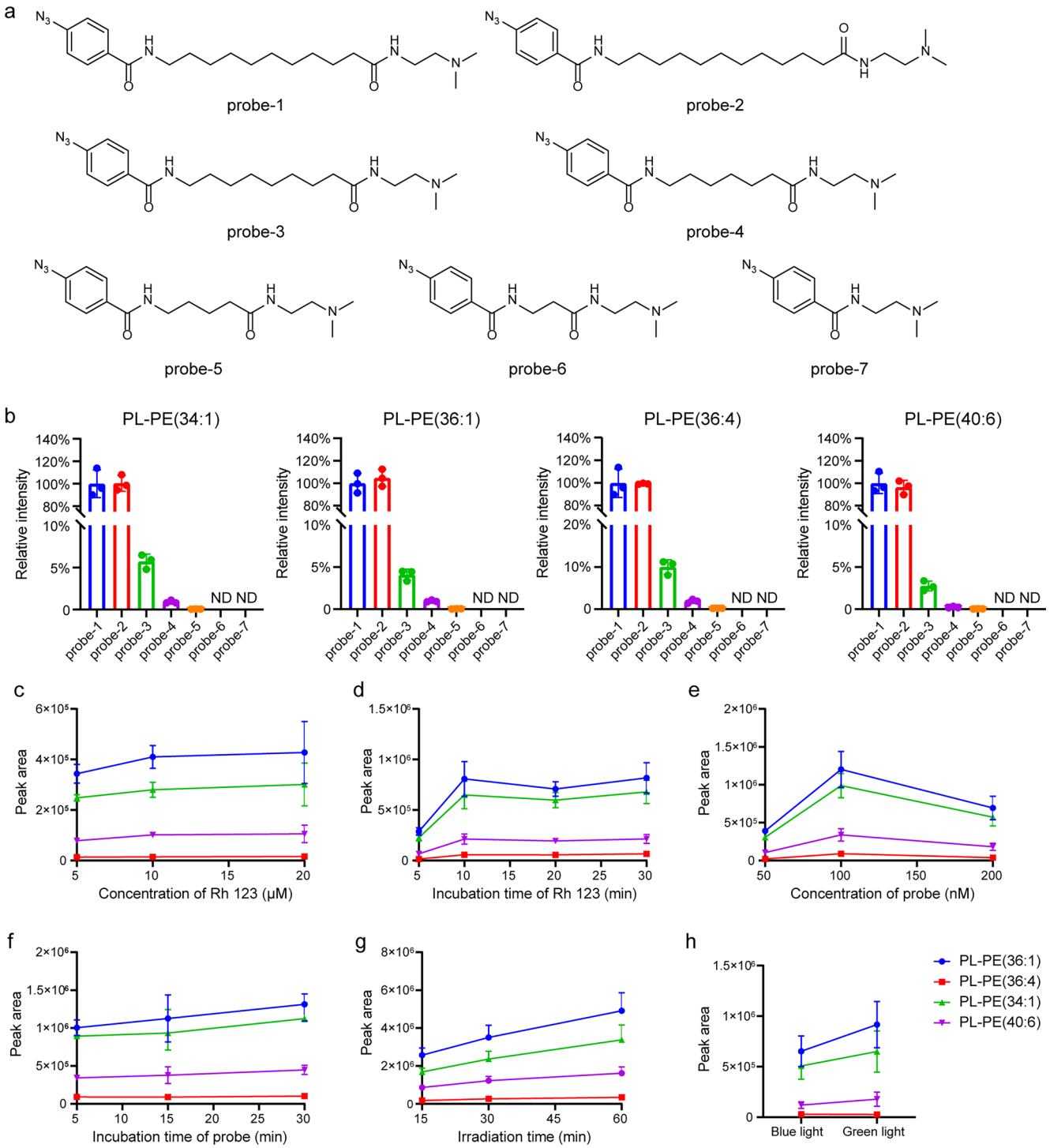

Extended Data Fig. 2 | Assessment of factors influencing photocatalytic labeling. (**a**) Structures of probes with different lengths of hydrophobic linkers; (**b**) Relative intensity of four PL-lipids using different probes listed in (**a**); (**c-h**) The effects of photosensitizer concentration (**c**) and incubation time (**d**), probe concentration (**e**) and incubation time (**f**), illumination time (**g**), and illumination wavelength (**h**) on the peak areas of PL-lipids. Bar plots represent mean ± s.d. (n=3 biologically independent replicates per group).

https://doi.org/10.1038/s41557-025-01886-w

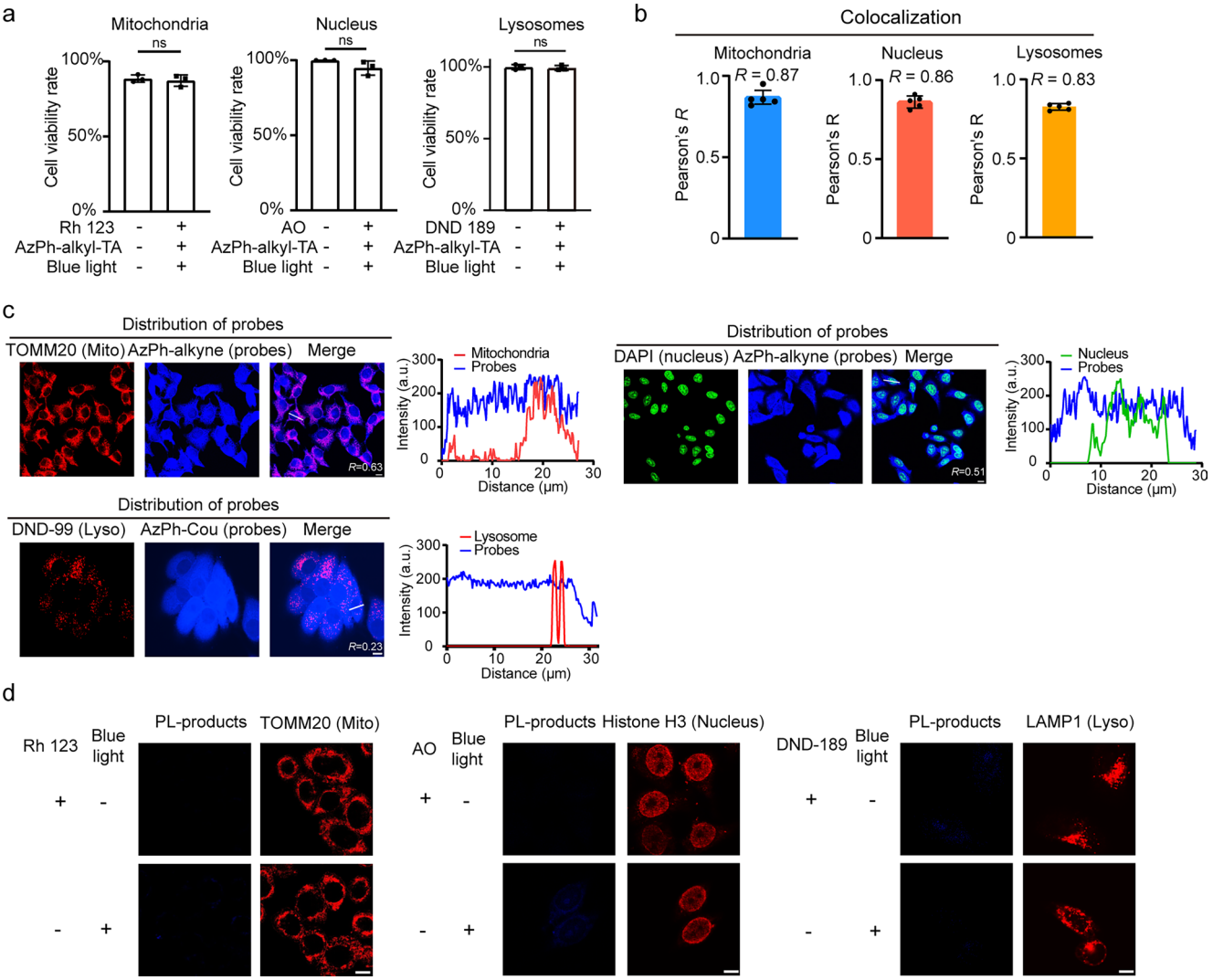

Extended Data Fig. 3 | Evaluation of biocompatibility and subcellular localization of proximity labeling of lipids. (**a**) Cytotoxicity under mitochondria-specific, nucleus-specific, and lysosome-specific photocatalytic labeling of lipids, respectively. Bar plots represent mean ± s.d. (n=3 biologically independent replicates per group; two-tailed Student's *t*-test). (**b**) Pearson's *R* values for evaluating the subcellular co-localization of mitochondria-specific, nucleus-specific, and lysosome-specific proximity labeling in living cells, respectively. Bar plots represent mean ± s.d. (n=5 biologically independent replicates per group). (**c**) Fluorescent images of labeling probes and their co-localization with mitochondria, nucleus, and lysosomes, respectively (Scale bar = 10 μm). (**d**) Fluorescent images of mitochondria (Mito)-specific, nucleus-specific, and lysosome (Lyso)-specific proximity labeling of lipids under different conditions in HeLa cells, respectively (Scale bar = 10 μm).

https://doi.org/10.1038/s41557-025-01886-w

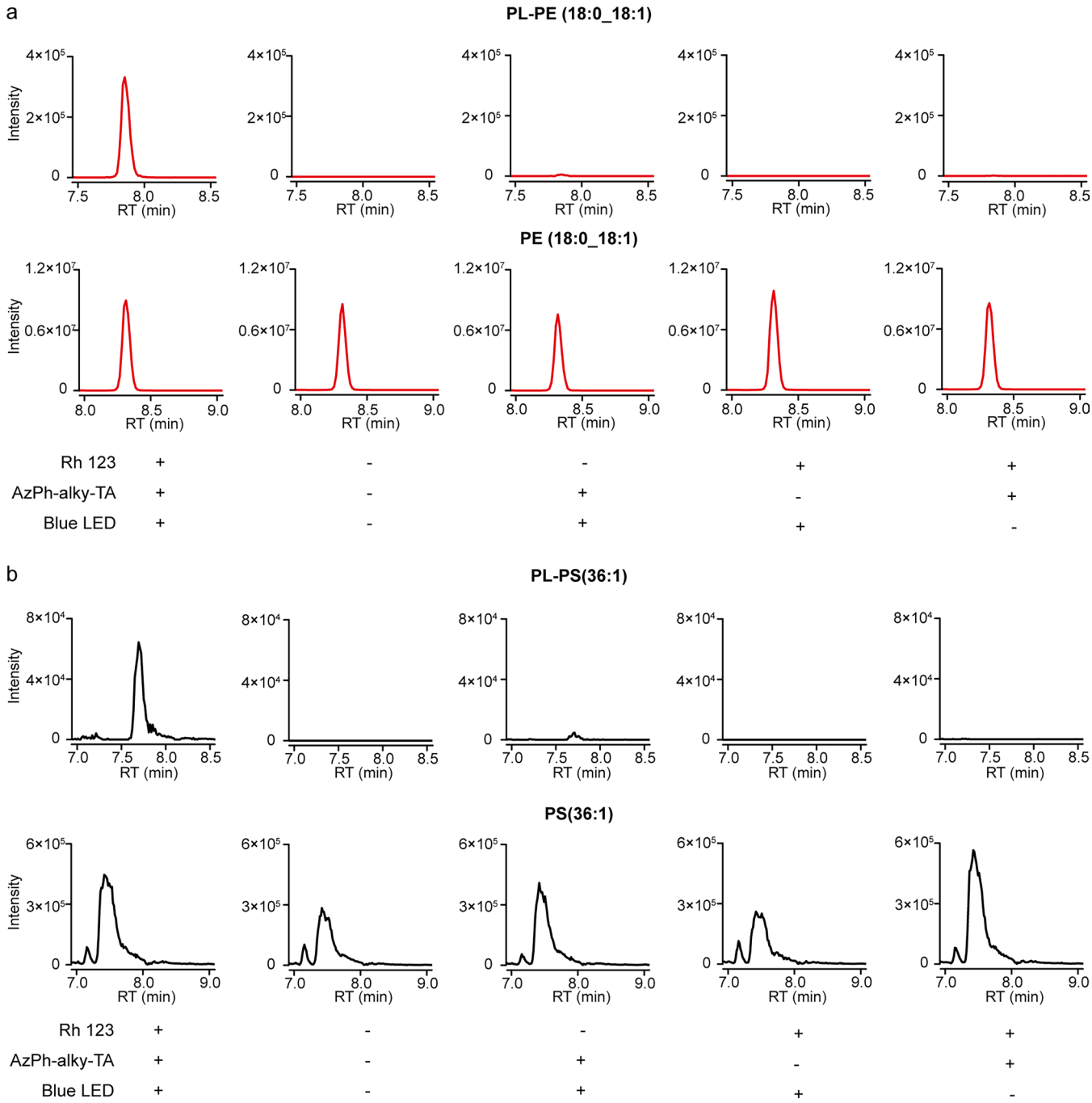

Extended Data Fig. 4 | Photocatalytic labeling of lipids under different conditions in HeLa cells. (**a**) Intensities of PL-PE(18:0_18:1) (upper panel) and PE(18:0_18:1) (lower panel); (**b**) Intensities of PL-PS(36:1) (upper panel) and PS(36:1) (lower panel).

https://doi.org/10.1038/s41557-025-01886-w

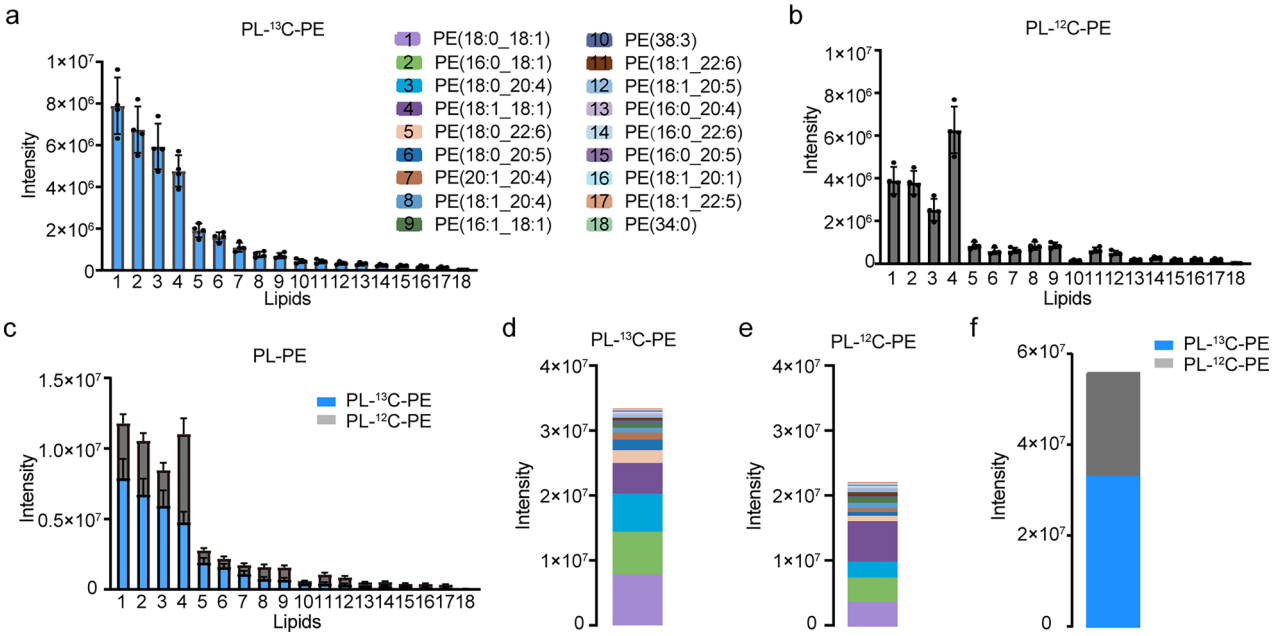

Extended Data Fig. 5 | Contribution of the PSD pathway to PE lipid pool in mitochondria. (**a**) Intensities of newly synthesized PE lipids via the PSD pathway (PL-^{13}C-PE) with [U-^{13}C]-serine labeling at 72 h; (**b**) Intensities of unlabeled PE lipids from other pathways (PL-^{12}C-PE) with [U-^{13}C]-serine labeling at 72 h; (**c**) Sum intensities of PL-^{13}C-PE and PL-^{12}C-PE for each PE lipid with [U-^{13}C]-serine labeling at 72 h; (**d**) Stacked sum intensity of 18 newly synthesized PE lipids via the PSD pathway (PL-^{13}C-PE) with [U-^{13}C]-serine labeling at 72 h. (**e**) Stacked sum intensity of 18 PE lipids from other pathways (PL-^{12}C-PE) with [U-^{13}C]-serine labeling at 72 h; (**f**) Sum intensity of 18 PE lipids in mitochondria via the PSD pathway (PL-^{13}C-PE) and other pathways (PL-^{12}C-PE) with [U-^{13}C]-serine labeling at 72 h, which was used to calculate the relative contribution percentages in Fig. 3h. Bar plots represent mean ± s.d. (n=4 biologically independent replicates).

https://doi.org/10.1038/s41557-025-01886-w

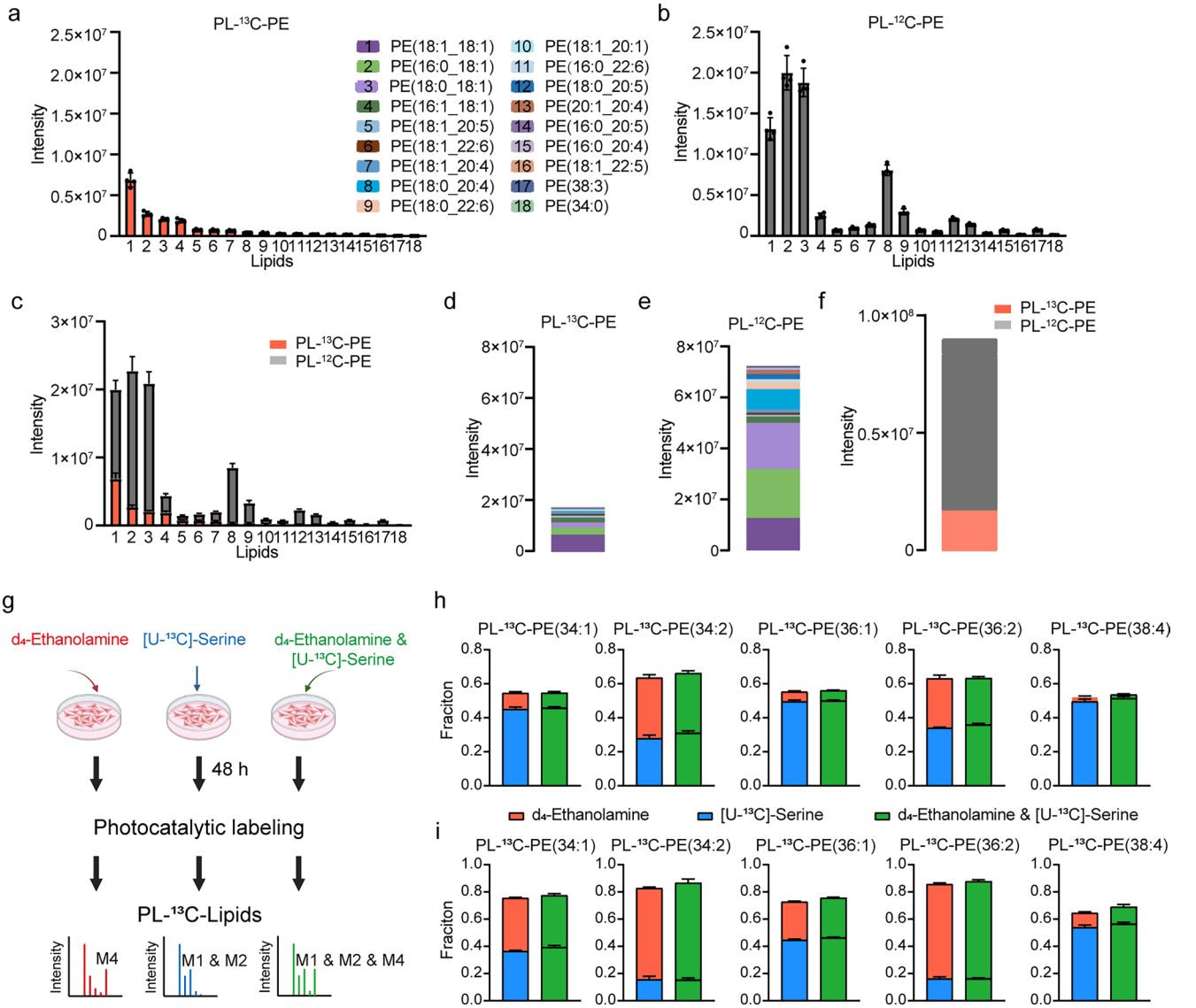

Extended Data Fig. 6 | Contribution of the CDP-Etn pathway to PE lipid pool in mitochondria. (**a**) Intensities of newly synthesized PE lipids via the CDP-Etn pathway (PL-^{13}C-PE) with [U-^{13}C]-Etn labeling at 72 h; (**b**) Intensities of PE lipids from other pathways (PL-^{12}C-PE) with [U-^{13}C]-Etn labeling at 72 h; (**c**) Sum intensities of PL-^{13}C-PE and PL-^{12}C-PE for each PE lipid with [U-^{13}C]-Etn labeling at 72 h; (**d**) Stacked sum intensity of 18 newly synthesized PE lipids via the CDP-Etn pathway (PL-^{13}C-PE) with [U-^{13}C]-Etn labeling at 72 h. (**e**) Stacked sum intensity of 18 PE lipids from other pathways (PL-^{12}C-PE) with [U-^{13}C]-Etn labeling at 72 h. (**f**) Sum intensity of 18 PE lipids in mitochondria via CDP-Etn pathway (PL-^{13}C-PE) and other pathways (PL-^{12}C-PE) with [U-^{13}C]-Etn labeling at 72 h, which was used to calculate the relative contribution percentages in Fig. 4i. Bar plots represent mean ± s.d. (n=4 biologically independent replicates in panels **a-f**). (**g**) Illustrations of single tracer labeling with either d_4-Ethanolamine or [U-^{13}C]-serine, as well as multi-labeling with both d_4-Ethanolamine and [U-^{13}C]-serine. (**h,i**) Comparison of the cumulative results from individual tracer labeling with those from simultaneous multi-tracer labeling with mitochondria-specific photocatalytic labeling (**h**) or nucleus-specific photocatalytic labeling (**i**), respectively. Bar plots represent mean ± s.d. (n=4 biologically independent replicates in panels **h-i**).

https://doi.org/10.1038/s41557-025-01886-w

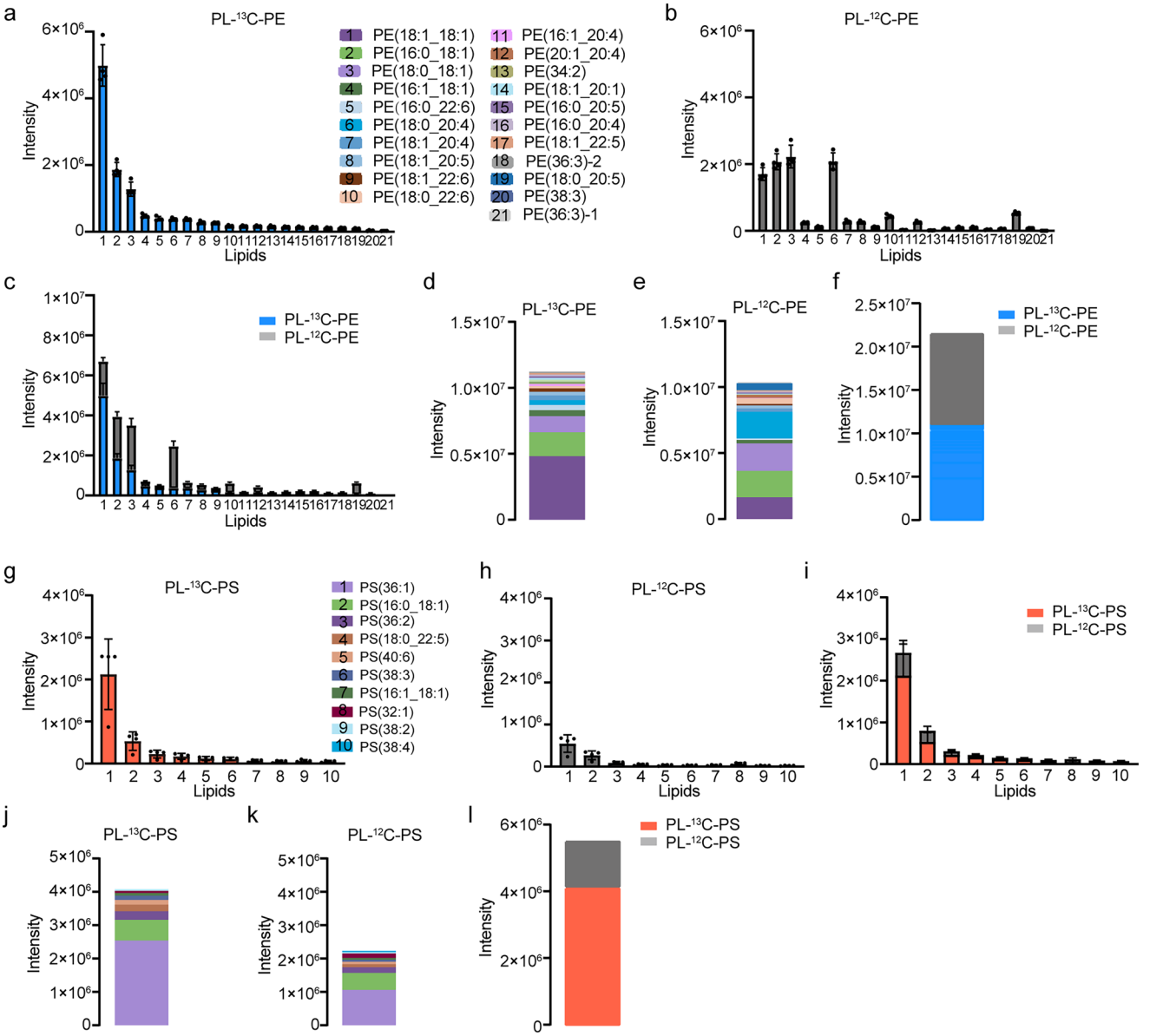

Extended Data Fig. 7 | Contribution of the CDP-Etn pathway to PE lipid pool and head-exchange reactions to PS lipid pool in nucleus. (**a**) Intensities of newly synthesized PE lipids via the CDP-Etn pathway (PL-^{13}C-PE) with [U-^{13}C]-Etn labeling at 72 h; (**b**) Intensities of PE lipids from other pathways (PL-^{12}C-PE) with [U-^{13}C]-Etn labeling at 72 h; (**c**) Sum intensities of both PL-^{13}C-PE and PL-^{12}C-PE for each PE lipid with [U-^{13}C]-Etn labeling with [U-^{13}C]-Etn labeling at 72 h; (**d**) Stacked sum intensities of 21 newly synthesized PE lipids via the CDP-Etn pathway (PL-^{13}C-PE) with [U-^{13}C]-Etn labeling at 72 h. (**e**) Stacked sum intensity of 21 PE lipids from other pathways (PL-^{12}C-PE) with [U-^{13}C]-Etn labeling at 72 h. (**f**) Sum intensity of 21 PE lipids in nucleus via CDP-Etn pathway (PL-^{13}C-PE) and other pathways (PL-^{12}C-PE) with [U-^{13}C]-Etn labeling at 72 h, which was used to calculate the relative contribution percentages in Fig. 5e. (**g**) Intensities of newly synthesized PS lipids via the head-exchange reaction in ER (PL-^{13}C-PS) with [U-^{13}C]-serine labeling at 72 h; (**h**) Intensities of PS lipids from other pathways (PL-^{12}C-PS) with [U-^{13}C]-serine labeling at 72 h; (**i**) Stacked sum intensities of both PL-^{13}C-PS and PL-^{12}C-PS of each PS lipid with [U-^{13}C]-serine labeling at 72 h; (**j**) Stacked sum intensity of 10 PS lipids from head-exchange reaction (PL-^{13}C-PS) with [U-^{13}C]-serine labeling at 72 h. (**k**) Stacked sum intensity of 10 PS lipids from other pathways (PL-^{12}C-PS) with [U-^{13}C]-serine labeling at 72 h. (**l**) Sum intensity of 10 PS lipids in nucleus via the head-exchange reaction (PL-^{13}C-PS) and other pathways (PL-^{12}C-PE) with [U-^{13}C]-serine labeling at 72 h, which was used to calculate the relative contribution percentages in Fig. 5j. Bar plots represent mean ± s.d. (n=4 biologically independent replicates).

https://doi.org/10.1038/s41557-025-01886-w

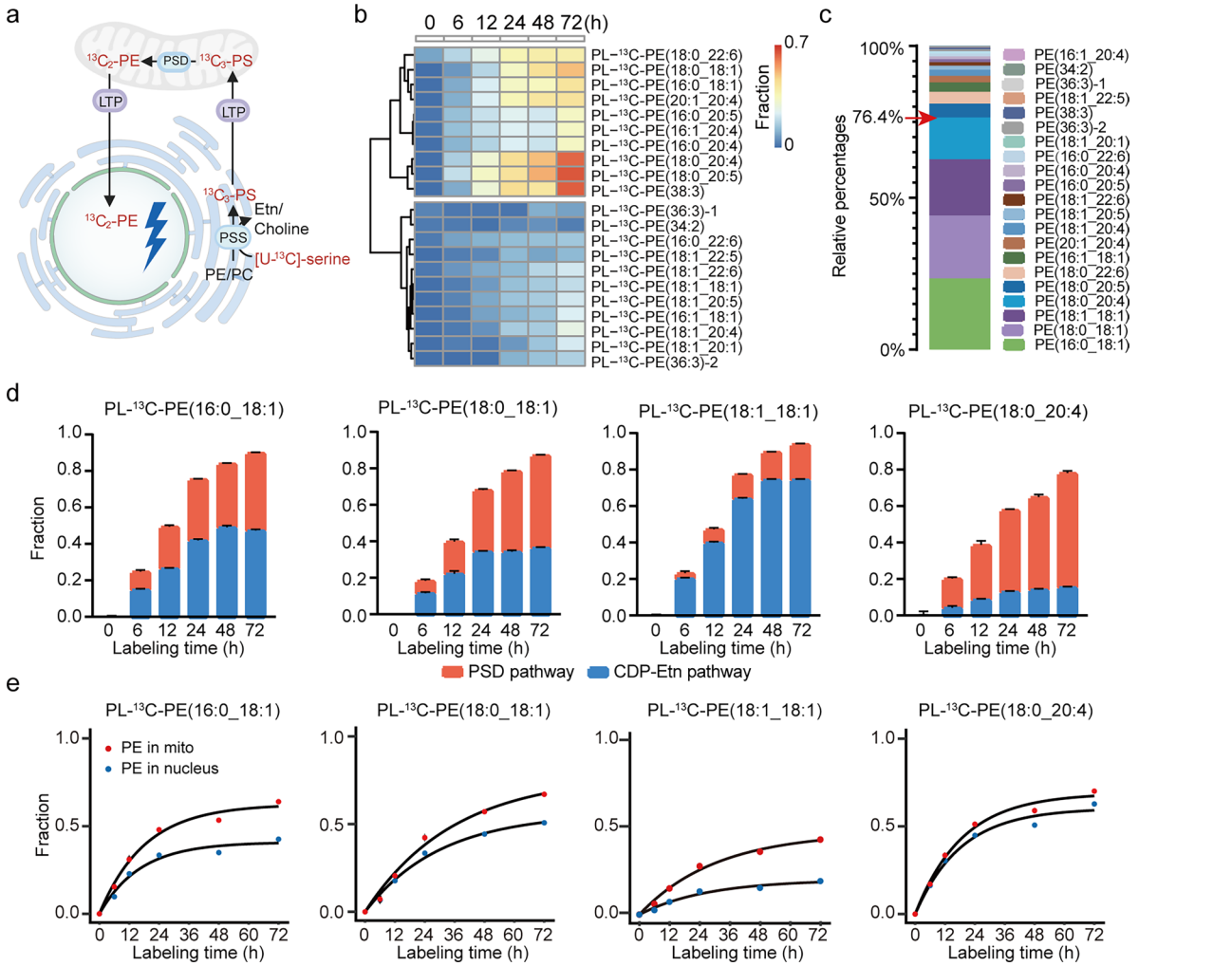

Extended Data Fig. 8 | Quantitative profiling of PE lipids in nucleus originated from PS lipids via the PSD pathway. (**a**) Schematic illustration of potentially indirect PE transport route from ER to nucleus. (**b**) Hierarchical clustering analysis of 21 dual-labeled PE lipids (PL-^{13}C-PE) accumulated in nucleus of HeLa cells. (**c**) Relative percentages of newly synthesized PE lipids in nucleus biosynthesized from PS lipids via PSD pathway. (**d**) The integrated accumulations of PE lipids originated from the PSD pathway and the CDP-Etn pathway. Bar plots represent mean ± s.d. (n=4 biologically independent replicates). (**e**) Comparisons of turnover rates and maximum turnover fractions of the four predominant PE lipids in nucleus and mitochondria via the PSD pathway. The dot represents the median value from four biologically independent replicates.

https://doi.org/10.1038/s41557-025-01886-w

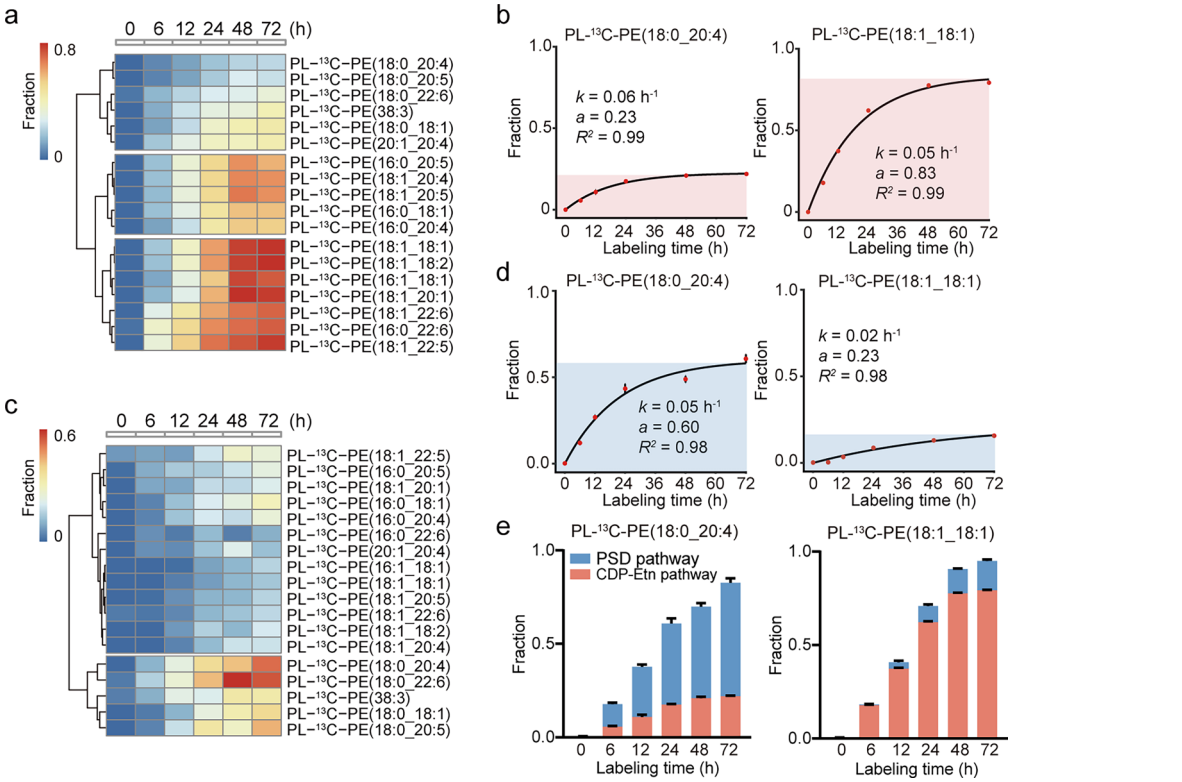

Extended Data Fig. 9 | Quantitative profiling of lipid turnover from ER and mitochondria to lysosomes. (**a**) Hierarchical clustering analysis of 18 dual-labeled PE lipids (PL-^{13}C-PE) via CDP-Etn pathway accumulated in lysosomes of HeLa cells. (**b**) The quantitative fit of the turnover kinetics of newly synthesized PE lipids via CDP-Etn pathway in lysosomes using the first-order exponential function. (**c**) Hierarchical clustering analysis of 18 dual-labeled PE lipids (PL-^{13}C-PE) via PSD pathway accumulated in lysosomes of HeLa cells. (**d**) The quantitative fit of the turnover kinetics of newly synthesized PE lipids via PSD pathway in lysosomes using the first-order exponential function. (**e**) The integrated accumulations of PE lipids originated from the PSD pathway and CDP-Etn pathway. Bar plots represent mean ± s.d. (n=4 biologically independent replicates).

nature portfolio

Corresponding author(s): Zheng-Jiang Zhu

Last updated by author(s): Jun 19, 2025

Reporting Summary

Nature Portfolio wishes to improve the reproducibility of the work that we publish. This form provides structure for consistency and transparency in reporting. For further information on Nature Portfolio policies, see our Editorial Policies and the Editorial Policy Checklist.

Statistics

For all statistical analyses, confirm that the following items are present in the figure legend, table legend, main text, or Methods section.

n/a	Confirmed
☐	☒ The exact sample size (*n*) for each experimental group/condition, given as a discrete number and unit of measurement
☐	☒ A statement on whether measurements were taken from distinct samples or whether the same sample was measured repeatedly
☐	☒ The statistical test(s) used AND whether they are one- or two-sided *Only common tests should be described solely by name; describe more complex techniques in the Methods section.*
☒	☐ A description of all covariates tested
☐	☒ A description of any assumptions or corrections, such as tests of normality and adjustment for multiple comparisons
☐	☒ A full description of the statistical parameters including central tendency (e.g. means) or other basic estimates (e.g. regression coefficient) AND variation (e.g. standard deviation) or associated estimates of uncertainty (e.g. confidence intervals)
☐	☒ For null hypothesis testing, the test statistic (e.g. *F*, *t*, *r*) with confidence intervals, effect sizes, degrees of freedom and *P* value noted *Give P values as exact values whenever suitable.*
☒	☐ For Bayesian analysis, information on the choice of priors and Markov chain Monte Carlo settings
☒	☐ For hierarchical and complex designs, identification of the appropriate level for tests and full reporting of outcomes
☐	☒ Estimates of effect sizes (e.g. Cohen's *d*, Pearson's *r*), indicating how they were calculated

Our web collection on statistics for biologists contains articles on many of the points above.

Software and code

Policy information about availability of computer code

Data collection	These tools were used in data collection: Analyst TF Software (Version 1.7.1, Sciex, USA), Bruker Compass HyStar (Version 6.0.30.0, Bruker Daltonics, Germany).
Data analysis	ProteoWizard (Version 3.0.6428), R package "XCMS" (Version 1.46.0), Skyline software (version 22.2.0.351), R package “Accucor” (version 0.2.4), R package ”stats” (version 3.6.1), Lipid4DAnalyzer (http://lipid4danalyzer.zhulab.cn/).

For manuscripts utilizing custom algorithms or software that are central to the research but not yet described in published literature, software must be made available to editors and reviewers. We strongly encourage code deposition in a community repository (e.g. GitHub). See the Nature Portfolio guidelines for submitting code & software for further information.

Data

Policy information about availability of data

All manuscripts must include a data availability statement. This statement should provide the following information, where applicable:

- Accession codes, unique identifiers, or web links for publicly available datasets
- A description of any restrictions on data availability
- For clinical datasets or third party data, please ensure that the statement adheres to our policy

Unless otherwise stated, all data supporting the results of this study can be found in the article, supplementary, and source data files. The raw LC-MS data files

generated in this study have been deposited in the National Omics Data Encyclopedia under accession code OEP00004920 (https://www.biosino.org/node/project/detail/OEP00004920). Source data are provided with this paper.

Human research participants

Policy information about studies involving human research participants and Sex and Gender in Research.

Reporting on sex and gender	No human participant is involved in this study.
Population characteristics	No human participant is involved in this study.
Recruitment	No human participant is involved in this study.
Ethics oversight	No human participant is involved in this study.

Note that full information on the approval of the study protocol must also be provided in the manuscript.

Field-specific reporting

Please select the one below that is the best fit for your research. If you are not sure, read the appropriate sections before making your selection.

☒ Life sciences ☐ Behavioural & social sciences ☐ Ecological, evolutionary & environmental sciences

For a reference copy of the document with all sections, see nature.com/documents/nr-reporting-summary-flat.pdf

Life sciences study design

All studies must disclose on these points even when the disclosure is negative.

Sample size	Datasets acquired in this study were performed on 3-6 biological replicates per group to demonstrate replication of biological results. These replicates were chosen because they are the commonly used number for most biological studies.
Data exclusions	At the 48-hour time point in Figure 3, three biologically independent replicates were available for analysis due to the loss of one sample.
Replication	All experiments were repeated at least three times using independently cultured cells, yielding consistent results to ensure reproducibility. Data analysis was conducted in an automated and unbiased manner. All findings were independently replicated. The micrographs shown are representative images.
Randomization	For all datasets, samples were assigned randomly to acquire LC-MS data.
Blinding	The investigators were blinded to group allocation during data collection. At the time of sample acquisition and processing, scientists were completely unaware of the sample group. The data analyses were blinded.

Reporting for specific materials, systems and methods

We require information from authors about some types of materials, experimental systems and methods used in many studies. Here, indicate whether each material, system or method listed is relevant to your study. If you are not sure if a list item applies to your research, read the appropriate section before selecting a response.

Materials & experimental systems

n/a	Involved in the study
☐	☒ Antibodies
☐	☒ Eukaryotic cell lines
☒	☐ Palaeontology and archaeology
☒	☐ Animals and other organisms
☒	☐ Clinical data
☒	☐ Dual use research of concern

Methods

n/a	Involved in the study
☒	☐ ChIP-seq
☒	☐ Flow cytometry
☒	☐ MRI-based neuroimaging

Antibodies

Antibodies used	The following antibodies were used in this study: Rabbit anti TOM20 (11802-1-AP, Proteintech), Rabbit anti VPS13A (28618-1-AP,

Antibodies used	Proteintech), Rabbit anti PDZD8 (PA5-46771, Invitrogen), Rabbit ant Histone H3(17168-1-AP, Proteintech), Mouse anti LAMP1 (67300-1-Ig, Proteintech).
Validation	All primary antibodies used in this study were commercially available and have been validated by manufacturer.Antibody validations and validation criteria are available on the following websites : anti TOM20 https://www.ptglab.com/results?category=&filter=&q=11802-1-AP anti VPS13A https://www.ptglab.com/results?category=&filter=&q=28618-1-AP anti PDZD8 https://www.thermofisher.cn/cn/zh/antibody/product/PDZD8-Antibody-Polyclonal/PA5-46771 anti-Histone H3 https://www.ptgcn.com/Products/Histone-H3-Antibody-17168-1-AP.htm anti-LAMP1 https://www.ptgcn.com/products/CD107a-Antibody-67300-1-Ig.htm

Eukaryotic cell lines

Policy information about cell lines and Sex and Gender in Research

Cell line source(s)	HeLa cell line (American Type Culture Collection); MEF cell line (American Type Culture Collection)
Authentication	The HeLa cell line used in this study were authenticated by short tandem repeat (STR) analysis.
Mycoplasma contamination	The cell lines were routinely tested for mycoplasma contamination. The cell lines used are free of mycoplasma but not described in text.
Commonly misidentified lines (See ICLAC register)	No Commonly misidentified lines were used.